

c-C₃H₂ deuteration towards prestellar and starless cores in the Perseus Molecular Cloud

J. Ferrer Asensio,¹ S. Scibelli,² * L. Steffes,⁵ B. Kulterer,³ A. Pokorny-Yadav,^{2,4} Y. Shirley,⁵ A. Megías,⁶ I. Jiménez-Serra,⁶ A. Taillard⁶

¹ RIKEN Cluster for Pioneering Research, Wako-shi, Saitama, 351-0106, Japan

² National Radio Astronomy Observatory, 520 Edgemont Road, Charlottesville, VA 22903, USA

³ Department of Astronomy, University of Virginia, 530 McCormick Rd, Charlottesville, Virginia 22904, USA

⁴ Department of Astronomy, University of California, Berkeley, Berkeley, CA, 94720, USA

⁵ Steward Observatory, University of Arizona, 933 North Cherry Avenue, Tucson, AZ 85721, USA

⁶ Centro de Astrobiología (CAB), CSIC-INTA, Carretera de Ajalvir, km 4, E-28805 Torrejón de Ardoz, Spain

Received ; accepted

ABSTRACT

Context. In cores deuterium fractionation becomes highly efficient due to low temperatures and CO freeze-out. Cyclopropenylidene (c-C₃H₂), a small cyclic molecule formed early in chemical evolution, and its deuterated forms serve as valuable tracers of gas-phase deuteration in these environments.

Aims. In order to statistically explore the c-C₃H₂ deuteration ratios towards starless and prestellar cores, we present observations of c-C₃H₂ and its deuterated isotopologues on a sample of cores in the Perseus Molecular Cloud.

Methods. Transitions of c-C₃H₂, c-C₃HD and c-C₃D₂ were observed with the Yebes 40m, the Arizona Radio Observatory (ARO) 12m and the Institut de Radioastronomie Millimétrique (IRAM) 30 meter telescopes towards a total of 16 starless and prestellar cores in the Perseus Molecular Cloud. The lines were fitted with Gaussian profiles and their column densities were computed using the non-LTE software RADEX.

Results. The main isotopologue c-C₃H₂ is detected in 93% (14/15) of the targeted cores (for one of the 16 cores none of its transitions were covered), its singly-deuterated form c-C₃HD is detected in 94% (15/16) of the targeted cores and its doubly-deuterated form c-C₃D₂ is detected towards 56% (9/16) of the cores detected. A range of column densities towards the different cores was derived to be: for c-C₃H₂, $(0.5 - 8.1) \times 10^{13} \text{ cm}^{-2}$; for c-C₃HD, $(0.2 - 2.1) \times 10^{12} \text{ cm}^{-2}$ and for c-C₃D₂, $(0.6 - 1.6) \times 10^{11} \text{ cm}^{-2}$. The ortho-to-para ratio of c-C₃H₂ was obtained for all except one core with a median value of 3.5 ± 0.4 . The D/H and D₂/D ratios were obtained for the cores with detections, yielding a statistically corrected D/H range of 0.5 - 9.2% with a median value of $1.5 \pm 0.2 \%$ and a statistically corrected D₂/D range 9.0 - 55.2% with a median value of $25.9 \pm 4.3 \%$.

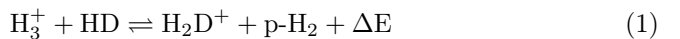
Conclusions. No apparent trend is seen with ortho-to-para ratio of c-C₃H₂ and the evolutionary stage of the core, as traced by volume density n_{H_2} . The median c-C₃H₂ D/H ratio in Perseus' starless cores appears lower than the value for the Taurus Molecular Cloud and Chamaeleon Molecular Cloud. The D₂/D ratio is equivalent between the Perseus and Taurus Molecular Clouds within uncertainties. There is a correlation with the D/H ratio and the n_{H_2} of the cores in Perseus, strengthening the idea of D/H being a tracer of core evolution. The D₂/D ratio does not correlate with n_{H_2} , but positively correlates with T_{kin} , suggesting that its formation is favoured by a slightly endothermic reaction.

Key words. ISM: molecules - ISM: clouds - radio lines: ISM - stars: formation - radiative transfer

1. Introduction

The deuterium to hydrogen ratio (D/H) in the local interstellar medium (ISM) is $2.0 \pm 0.1 \times 10^{-5}$ (Linsky 2003; Prodanović et al. 2010; Caselli et al. 2012; Cecarelli et al. 2014). Locally, molecules can be enriched with deuterium resulting in higher D/H ratios compared to the value observed in the local ISM. This process, known as deuterium fractionation, happens efficiently in prestellar cores. These cores, that represent the earliest stage of the star formation process, are gravitationally bound objects which show signs of contraction motions

and are characterised by high volume densities ($n_{\text{H}_2} \sim 10^6 \text{ cm}^{-3}$) and low temperatures ($T < 10 \text{ K}$) at their centres (Bergin & Tafalla 2007; Keto & Caselli 2008). These are a subgroup of starless cores, which are also defined as gravitationally bound objects, but do not show signs of contraction motions. The low temperatures favour the formation of bonds with deuterium over hydrogen due to the lower zero point energy (ZPE) of deuterium. Moreover, the two-way reaction involving one of the main deuteration agents in the gas phase, H₂D⁺:



is shifted to the right hand side because at low temperatures the backwards reaction is quenched (Pagani et al.

* Jansky Fellow of the National Radio Astronomy Observatory.

1992). This is due to the exothermicity of the reaction and the H₂ ortho-to-para (otp) ratio being low in prestellar cores (< 0.01; Pagani et al. 2009; Dislaire et al. 2012) compared to its statistical value of 3. The higher energy of ortho-H₂ with respect to para-H₂ can overcome the reaction barrier destroying H₂D⁺ in favour of H₃⁺. Furthermore, as the temperatures decrease towards the centre of the core and with the contraction of the core, the main destructor of H₂D⁺, CO, is frozen onto the surface of dust grains. All of these conditions increase the H₂D⁺/H₃⁺ ratio. Then, the H₂D⁺ can transfer the deuterium atom to other molecules.

Prestellar cores contract with time, which lowers the temperature at the centre as well as increases the area of CO freeze out. Thus, colder and longer-lived prestellar cores will present higher deuterium fractionation ratios as well as multi-deuterated molecules compared to warmer and shorter-lived ones. This was inferred from modelling methanol (CH₃OH) deuteration in prestellar cores using observed D/H and D₂/D ratios towards low and high-mass protostellar sources (van Gelder et al. 2022). Thus, the D/H and D₂/D molecular ratios are a great tool to better understand the characteristics of the prestellar core nature.

Nevertheless, because of the low temperatures of starless and prestellar cores, studying the deuteration of molecules larger than methanol is challenging due to low abundances. Even doubly deuterated methanol has only been reported in the literature for three cores (Lin et al. 2023; Scibelli et al. 2025). This is why, in this work we explore the deuterium fractionation in starless and pre-stellar cores by focusing on the deuteration of a smaller molecule, cyclopropenylidene (c-C₃H₂) towards the Perseus Molecular Cloud.

c-C₃H₂ is a small organic molecule detected towards multiple sources at different stages of the star formation process such as diffuse clouds, starless and prestellar cores, circumstellar envelopes, hot corinos, planetary nebulae, and outflow cavities (Thaddeus et al. 1985; Cox et al. 1988; Madden et al. 1989; Lucas & Liszt 2000; Martínez-Henares et al. 2025). Its deuterated forms have also been detected towards the interstellar medium (Bell et al. 1986; Gerin et al. 1987; Spezzano et al. 2013; Majumdar et al. 2017). Deuterated cyclopropenylidene has only been detected towards a handful of prestellar cores in Taurus: Gerin et al. (1987); Spezzano et al. (2013); Gratier et al. (2016); Chantzos et al. (2018); Giers et al. (2022) and in Chamaeleon: Lis et al. (2025). c-C₃H₂ is mainly formed by the radiative recombination of c-C₃H₃⁺ in the gas phase (Loison et al. 2017). c-C₃HD and c-C₃D₂ are formed from the successive deuteration of the main isotopologue, also in the gas phase (Spezzano et al. 2013). The singly- and doubly-deuterated c-C₃H₂ abundances towards the L1544 prestellar core can be reproduced by chemical models only using gas-phase reactions (Spezzano et al. 2013). This makes c-C₃H₂ a unique tracer for gas-phase only deuteration in contrast to, for example methanol, which is thought to form uniquely on the surface of grains (Watanabe & Kouchi 2002; Osamura et al. 2004; Watanabe et al. 2005; Fuchs et al. 2009; Hidaka et al. 2009).

Perseus is one of the nearest ($\sim 294 \pm 17$ pc; Zucker et al. 2018) and most extensively studied molecular clouds in the solar neighbourhood. Covering a total area

of about 74 pc² (Evans et al. 2009), the cloud extends roughly 10 pc across the sky and exhibits a velocity gradient with local standard of rest (LSR) velocities (v_{LSR}) ranging from 4.5 to 10 km s⁻¹, possibly indicating the superposition of multiple cloud components (Arce et al. 2010). Perseus is a low-mass star-forming region that hosts a rich population of young stellar objects (YSOs), including about 100 dense cores and over 400 YSOs, of which approximately 50 are classified as Class 0 and Class I protostars (Yang et al. 2021). The cloud contains two main protostellar clusters, NGC 1333 and IC 348, along with other regions of active star formation such as B5, B1, L1448, and L1455. This region harbours a large number of low-mass pre-main sequence stars, embedded protostars, and starless or prestellar cores (e.g., Ladd et al. 1993; Aspin et al. 1994; Lada & Lada 1995; Hatchell et al. 2005; Enoch et al. 2006; Kirk et al. 2006; Muench et al. 2007; Gutermuth et al. 2008; Evans et al. 2009). In particular, NGC 1333 exhibits numerous active molecular outflows, making it one of the most dynamically young and active subregions within the cloud. Recent chemical surveys of embedded protostars in Perseus, conducted with the Nobeyama telescope, have detected species such as C₂H, c-C₃H₂, and CH₃OH, revealing possible correlations between source location and the CH₃OH/C₂H ratio, which may reflect environmental influences on the chemical composition of these protostellar systems (Higuchi et al. 2018). Scibelli et al. (2024) surveyed 35 starless and prestellar cores in the Perseus Molecular Cloud with the ARO 12 m telescope, detecting methanol (CH₃OH) and acetaldehyde (CH₃CHO) in 100% and 49% of the sample, respectively. Follow-up Yebes 40 m observations revealed several additional complex organic molecules (COMs), showing that such species are already widespread in the cold gas preceding star and planet formation in Perseus. In this work we continue the chemical survey of the starless and prestellar cores of the Perseus Molecular Cloud focusing on c-C₃H₂ and its deuterated isotopologues.

This study is structured as follows: the observations are presented in Section 2, the description of the methodology used to reduce and fit the data are presented in Section 3, the results are presented in Section 4, these results are interpreted in Section 5, and we summarize the conclusion in Section 6. Moreover, supplementary information is collected in the Appendix.

2. Observations

Single pointing observations of c-C₃H₂, c-C₃HD and c-C₃D₂ towards fifteen Perseus cores were taken by two different telescopes: the Yebes Observatory 40m telescope and the Arizona Radio Observatory (ARO) 12m telescope. Additionally, supplemental data from the Institut de Radioastronomie Millimétrique 30 meter telescope (IRAM 30m) for one additional core is used, bringing the total number of cores to sixteen (Figure 1, Table 1). All of the transitions targeted are presented in Table 2.

The data taken by the Yebes 40m telescope was first presented in Scibelli et al. 2024. These observations were taken between 2022 and 2023 corresponding to the projects with ID 22A022 and 23A025 (PI: Scibelli). The fifteen Perseus cores targeted were selected on the basis of the detection of acetaldehyde (CH₃CHO) to search for

other complex organic molecules (COMs). These cores were observed with the Q-band wide-band receiver (Ter-cero et al. 2021) with a bandwidth of 18.5 GHz in the 31.5 – 50 GHz frequency range. The resolution of the observations is of 38.0 kHz (0.38 km s⁻¹ – 0.23 km s⁻¹). The beam ranges between 36" and 56" across the full frequency range. The data was reduced and converted to main beam temperature (T_{MB}) using the publicly available Python-based scripts¹ developed by Megías et al. 2023, which calls on the Continuum and Line Analysis Single-dish Software (CLASS), an application from the GILDAS² software (Pety 2005). For further information on the data and on the reduction process refer to Scibelli et al. 2024.

Moreover, to add additional transitions, we observed c-C₃H₂ and c-C₃HD transitions using the ARO 12-m Radio Telescope on Kitt Peak (PI: Steffes). Observations occurred over 46 shifts from February 21, 2025 through June 15, 2025 using absolute position switching for 30 seconds on and off source for 5 minute scans. Using the multi-window mode on AROWS, we observed two transitions of para-c-C₃H₂, these being the 2_{2,0} - 1_{1,1} (150.44 GHz) and the 4_{0,4} - 3_{1,3} (150.820665 GHz) transitions. Then, we observed two transitions of ortho-c-C₃H₂, these being the 4_{1,4} - 3_{0,3} (150.85 GHz) and the 3_{1,2} - 2_{2,1} (145.09 GHz) transitions. Finally, we observed two transitions of c-C₃HD. These were the 4_{1,4} - 3_{0,3} (136.370909 GHz) and 2_{2,0} - 1_{1,1} (137.454464 GHz) transitions. After applying Hanning smoothing, the velocity resolution ranged over 0.08 – 0.09 km s⁻¹ with a frequency resolution of 39.06 kHz. These observations had a beam size ranging from 41" to 46".

The length of the ARO 12m observations was determined by the amount of time required for each to achieve a signal-to-noise ratio (SNR) ≥ 5 . Because of the use of multi-window mode, this resulted in many observations achieving a SNR > 5 as we stayed on source in a given setup until the weakest transition achieved a SNR of 5. Several sources were simply too weak to achieve this sensitivity within the given time. Linear functions were then fit to all of the velocity channels not within the 5σ boundaries of the Gaussian. All of these observations were summed, weighted by $1/\sigma^2$ (with σ being the RMS noise level) and fit with a Gaussian using CLASS. These were then subtracted from the summed spectra to baseline them. The average beam efficiency for the 2mm frequency range of 81% was applied.

Additionally, we are including one c-C₃HD and one c-C₃D₂ transition observed towards another prestellar core in the Perseus Molecular Cloud, L1448. These observations were carried out with the Institut de Radioastronomie Millimétrique 30 meter telescope (IRAM 30m) within the project with ID IRAM 071-23 (PI: Fuente, Kulterer et al. (2025)). The observations were carried out on the 2nd and 3rd of May 2024 in excellent weather (PWV = 0–4.6 mm, $\tau < 0.1$) and at a system temperature (T_{sys}) of 60–130 K. EMIR with the FTS backend and a spectral resolution of 49 kHz was used. The data were taken in frequency-switching mode with a frequency throw of 3.9 MHz. Of the four original spectral windows,

those centred on 93.6 and 106.1 GHz, with rms of 2.13 and 2.20 mK, were used. The half power beam width (HPBW) of c-C₃HD 3_{0,3} - 2_{0,2} is 23" and the one for the c-C₃D₂ 3_{0,3} - 2_{1,2} transition is 26".

3. Analysis

The observations were fit with the Python "pyspeckit" package (Ginsburg & Mirocha 2011; Ginsburg et al. 2022). For three transitions, c-C₃H₂ 3_{2,1} - 3_{1,2}, c-C₃D₂ 1_{1,1} - 0_{0,0} for the core Per799, c-C₃D₂ 1_{1,1} - 0_{0,0} for the core Per627, the fit resulted in anomalously large errors for the V_{LSR} and the full width half maximum (FWHM). The limited spectral resolution of the Yebes 40m observations, which ranges between 0.23 and 0.38 km s⁻¹ compared to the 0.08 – 0.09 km s⁻¹ of the ARO 12m and 0.14–0.16 km s⁻¹ of the IRAM 30m observations, does not allow to resolve these lines, which appear narrower than the rest. For these three transitions the area under the line is directly derived from the spectra with a Python routine, and then by assuming a fixed line width, the peak temperatures are calculated and printed in Tables A.1 and A.3 alongside an asterisk (*). A transition is considered detected if its peak temperature is $\geq 3\sigma$. The c-C₃H₂ and c-C₃HD isotopologues are considered detected towards a core if multiple transitions were detected. In the case of c-C₃D₂, we consider that if the main and D-isotopologues have been detected towards a specific core, and we have at least one detected c-C₃D₂ transition, this isotopologue is also detected.

For the derivation of the column density, it should be noted that both c-C₃H₂ and c-C₃D₂ have ortho and para states. Because the interconversion timescales within these states are long, ortho and para states can be treated as separate molecules. Thus, the total column density of c-C₃H₂ is the column density of ortho-c-C₃H₂ plus the column density of para-c-C₃H₂. The same applies to c-C₃D₂. For more information, refer to Section 4.1.1.

The column densities for the different isotopologues were calculated using the RADEX code (van der Tak, F. F. S. et al. 2007). RADEX is a non-LTE radiative transfer code that requires physical information about the source, volume density (n_{H_2}) and kinetic temperature (T_{kin}), as well as spectral and collisional rate information of the molecule to model its transitions.

The input n_{H_2} , and T_{kin} used to model the line intensity, and subsequently constrain column densities, (see Table 1) are based on the median values for *Herschel* maps (Pezzuto et al. 2021) within the ARO 12m 62" beam. The data analysed in this study has different beam sizes owing to the use of different telescopes and different targeted frequencies. We take the derived volume densities listed in Scibelli et al. (2024) as their value does not significantly change when considering the different beam sizes in this study (see Section B in the Appendix). Additionally, we compute the n_{H_2} value for L1448 also with a *Herschel* map using a 62" beam, for comparison purposes. The T_{kin} values for different cores are constrained from NH₃ observations, except for Per615 where the *Herschel* T_{dust} is reported (see Scibelli et al. (2024) for details). The T_{kin} for L1448 is derived from far infrared and sub-millimetre observations (Zari et al. 2016; Rodríguez-Baras et al. 2021).

¹ <https://github.com/andresmegias/gildas-class-pipeline/>

² <https://www.iram.fr/IRAMFR/GILDAS/>

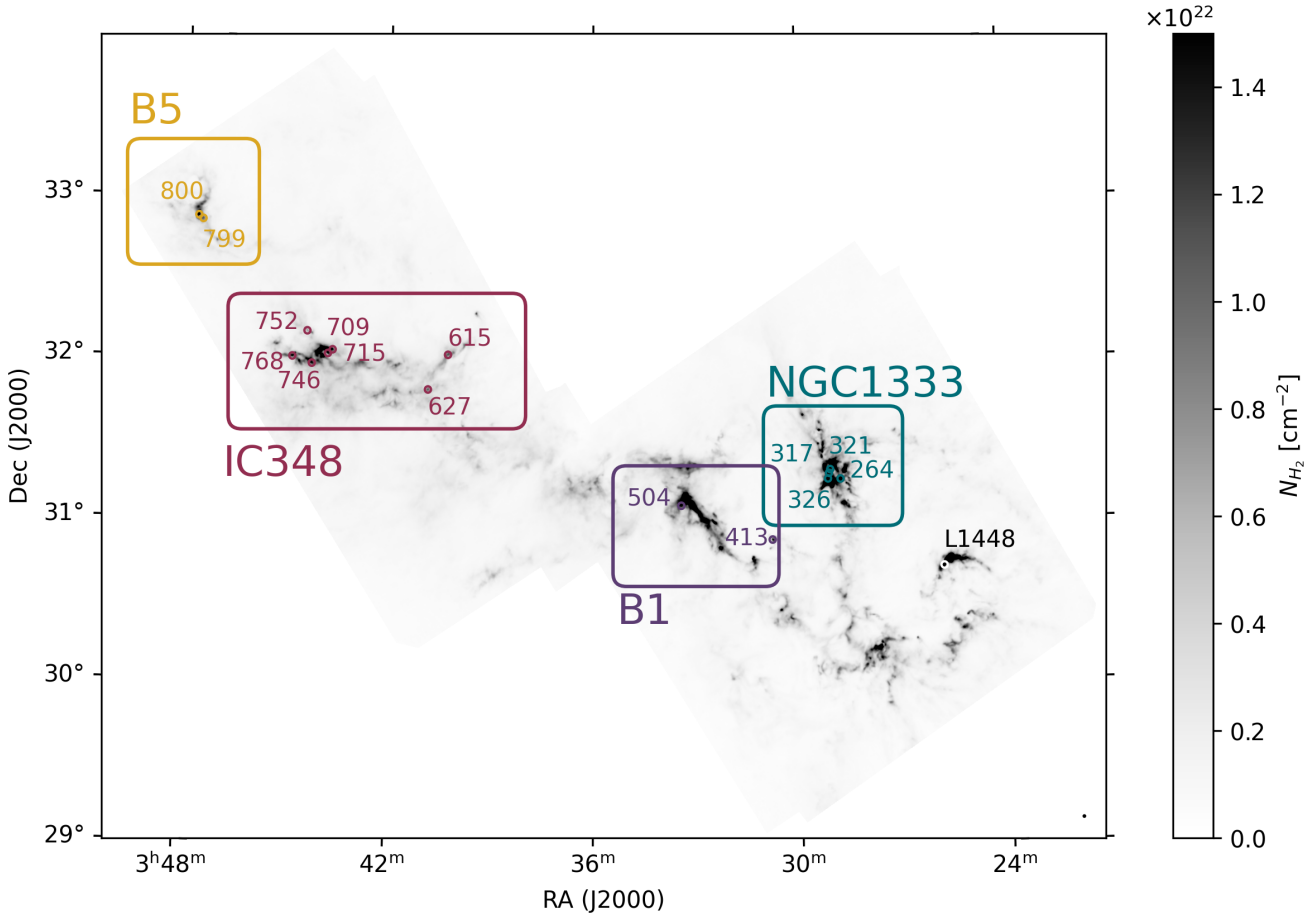


Fig. 1. Molecular hydrogen column density (N_{H_2}) map of the Perseus Molecular Cloud in gray scale (Pezzuto et al. 2012; Sadavoy et al. 2012, 2014). The starless and prestellar cores studied in this study are indicated by coloured circles corresponding to the regions within the molecular cloud where they are located. NGC1333 is plotted in teal, B1 in purple, IC348 in red and B5 in yellow.

For the three transitions where the pyspeckit fitting was not possible, the area extracted under the line was used alongside an assumed linewidth (0.5 km s^{-1}) to derive the line intensity. A 10% uncertainty was assumed for both n_{H_2} and T_{kin} (see Scibelli et al. (2024)). The column density values do not vary significantly for a sensible range of n_{H_2} and T_{kin} (for more information see Appendix B). The column density for each molecule (ortho- $\text{c-C}_3\text{H}_2$, para- $\text{c-C}_3\text{H}_2$, $\text{c-C}_3\text{HD}$, ortho- $\text{c-C}_3\text{D}_2$ and para- $\text{c-C}_3\text{D}_2$) was adjusted minimizing the χ^2 value. Uncertainties were estimated using a Monte Carlo approach in which the observed line parameters, n_{H_2} and T_{kin} were randomly perturbed within their respective uncertainties, and the RADEX fit was repeated for each trial. Lastly, the total column densities were calculated for $\text{c-C}_3\text{H}_2$ by summing the ortho and para column densities. In the case of $\text{c-C}_3\text{D}_2$ there are no ortho and para transitions observed towards the same source simultaneously, so a statistical ortho-to-para ratio value of 2 is used to compute the total column densities (see Section 4.1.1).

Finally, to explore possible correlations between the physical parameters of the cores and the derived column densities, otp ratios, D/H and D_2/D ratios we employ the Pearson correlation coefficient (r), which measures statistically the linear relationship between two variables.

4. Results

The parameters resulting from the Gaussian fitting of the observed $\text{c-C}_3\text{H}_2$, $\text{c-C}_3\text{HD}$ and $\text{c-C}_3\text{D}_2$ towards all of the cores (T_{MB} , V_{LSR} , FWHM and rms) can be found in Appendix A. The fitting of the transitions towards the Perseus cores can be seen in Figures 2, 3 and 4, except for core L1448 which is plotted in Figure 5. The number of detected transitions for each of the isotopologues towards each source is summarised in Table 3, and the total detection statistics, including detected, non-detected and non-targeted, are shown with pie charts in Figure 6.

The column densities for each of the isotopologues towards each of the cores, calculated following the method described in Section 3, are summarised in Table 4.

The results for each of the isotopologues, $\text{c-C}_3\text{H}_2$, $\text{c-C}_3\text{HD}$ and $\text{c-C}_3\text{D}_2$ are discussed in Sections 4.1, 4.2, 4.3, respectively. Moreover, the $\text{c-C}_3\text{H}_2$ ortho-to-para ratio and its deuteration ratios are presented in Subsections 4.1.1 and 4.4.

The plots related to $\text{c-C}_3\text{H}_2$, $\text{c-C}_3\text{HD}$ and $\text{c-C}_3\text{D}_2$ are plotted consistently through this study in blue, green and orange, respectively.

Table 1. Starless and prestellar cores in the Perseus Molecular Cloud targeted in this study.

Region	Core # ^a (<i>Herschel</i>)	RA (J2000)	DEC (J2000)	Distance ^b (pc)	N_{H_2} ($\times 10^{22} \text{ cm}^{-2}$)	n_{H_2} ($\times 10^5 \text{ cm}^{-3}$)	T_{kin} (K)
NGC1333	264	03:28:47.14	+31:15:11.4	294	2.06	0.75	10.8
	317	03:29:04.93	+31:18:44.4	294	2.63	0.96	13.6
	321	03:29:07.17	+31:17:22.1	294	3.65	1.33	12.6
	326	03:29:08.97	+31:15:17.2	294	7.88	2.87	12.3
B1	413	03:30:46.74	+30:52:44.8	297	1.17	0.42	10.5
	504	03:33:25.31	+31:05:37.5	297	1.80	0.65	9.7
IC348	615	03:40:14.92	+32:01:40.8	314	1.03	0.35	10.3
	627	03:40:49.53	+31:48:40.5	314	0.93	0.32	12.4
	709	03:43:38.06	+32:03:07.4	314	1.48	0.51	13.5
	715	03:43:46.34	+32:01:43.5	314	1.45	0.49	14.8
	746	03:44:14.38	+31:58:00.7	314	1.42	0.49	10.6
	752	03:44:23.10	+32:10:01.0	314	0.63	0.22	14.7
	768	03:44:48.83	+32:00:31.6	314	1.43	0.49	10.8
B5	799	03:47:31.31	+32:50:56.9	325	1.01	0.33	10.4
	800	03:47:38.97	+32:52:16.6	325	1.93	0.64	11.7
L1448 ^c		03:25:49.00	+30:42:24.6	285	10.6	0.57	15.1

Notes. ^a The cores are numbered in agreement with Pezzuto et al. (2021). ^b The distances of the cores are taken from Pezzuto et al. (2021). ^c The physical properties of L1448 were obtained through private communication related to the work of Rodríguez-Baras et al. (2021). The different subregions of the Perseus Molecular Cloud are colour coded to ease posterior analysis.

4.1. c-C₃H₂

For c-C₃H₂ a total of six lines were targeted: two at lower frequencies with the Yebes 40m telescope: 3₂₁ - 3₁₂ (o) and 2₁₁ - 2₀₂ (p); and four at higher frequencies with the ARO 12m telescope: 2₂₀ - 1₁₁ (p), 4₀₄ - 3₁₃ (p), 3₁₂ - 2₂₁ (o) and 4₁₄ - 3₀₃ (o). The additional ARO 12m observations were done a posteriori to have multiple ortho and para transitions with different E_{up} to be able to better constrain the excitation temperature and column density of c-C₃H₂. This molecule was not targeted towards L1448.

Out of the 15 cores where our data covers c-C₃H₂, we detected the molecule towards 14 cores ($\sim 93\%$). The SNR calculated from the line peak temperature, ranges from 3 to 86 for the detected transitions. The only core where c-C₃H₂ was not detected is Per752.

Note that some lines observed with the ARO 12m telescope towards Per709 have profiles that deviate from a Gaussian. This line profile is resolved for some of the transitions observed with the ARO 12m telescope, but not for the transitions observed with the Yebes 40m telescope, owing to their different spectral resolutions. The origin of this double-peaked line profiles are unknown. Because this profile is only marginally resolved in a few transitions, we do not attempt to model it. We note that this introduces some additional uncertainty in the column densities derived towards Per709.

The 3_{2,1}-3_{1,2} ortho transition could not be modelled with RADEX for core Per413. The c-C₃H₂ 3_{2,1}-3_{1,2} transition has quite a higher upper energy ($E_{\text{up}} \sim 30$ K) compared to the other ortho transitions. Per413 is the core where c-C₃H₂ is the most abundant (Figure C.1 in Appendix C). Thus, in Per413 this transition may be tracing warmer gas from the envelope at different n_{H_2} and T_{kin} and thus could not be fitted alongside the other ortho

transitions. This transition has been excluded from the column density calculation for Per413.

The column density of c-C₃H₂ was calculated using the method described in Section 3. The column densities for the ortho- and para-c-C₃H₂ were computed separately, as they have different collisional rate coefficients. The main isotopologue rate coefficients are given in Ben Khalifa et al. (2019), while the ones for the deuterated isotopologues are given in Ben Khalifa et al. (in prep.). Then, these obtained values are summed to give the total-c-C₃H₂ column density which we present in Table 4. For the core Per752, as c-C₃H₂ was not detected, we give an upper limit column density. This core was exclusively observed with the Yebes 40m data, and thus, the upper limit column density is estimated with just the 3_{2,1} - 3_{1,2} and 2_{1,1} - 2_{0,2} transitions. A line width of 0.5 km s⁻¹ was assumed. The total c-C₃H₂ column density values found range from $5.0 \pm 1.0 \times 10^{12} \text{ cm}^{-2}$ (Per317) to $8.1 \pm 1.8 \times 10^{13} \text{ cm}^{-2}$ (Per413), with a weighted average of $8.6 \pm 0.5 \times 10^{12} \text{ cm}^{-2}$ (not taking into account the upper limit of Per752).

The ortho-c-C₃H₂ excitation temperatures (T_{ex}) returned by RADEX are very similar amongst transitions and cores with a median of 3.7 K. The situation is similar for para-c-C₃H₂, where the T_{ex} has a median of 3.5 K. The optical depth (τ) of c-C₃H₂ changes for the different transitions. For 3_{2,1} - 3_{1,2}, τ has a median of 0.08, for 2_{1,1} - 2_{0,2} the median τ is 0.14, for 2_{2,0} - 1_{1,1} is 0.73, for 4_{0,4} - 3_{1,3} is 0.32, for 3_{1,2} - 2_{2,1} the median is 0.83 and for 4_{1,4} - 3_{0,3} the median is 1.27.

4.1.1. c-C₃H₂ ortho-to-para ratio

Molecules with symmetry that have two equivalent protons (or H atoms) exhibit two different type of states:

Table 2. Observed Molecular Transitions

Molecule	Transition	(o/p/-)	Frequency (MHz)	E_{up} (K)	A_{ij} ($\times 10^{-6} \text{ s}^{-1}$)
Yebes 40m					
c-C ₃ H ₂	3 ₂₁ - 3 ₁₂	o	44104.7769	30.85	3.20
	2 ₁₁ - 2 ₀₂	p	46755.6100	8.67	2.68
c-C ₃ HD	2 ₁₁ - 2 ₀₂	-	38224.4415	7.56	1.75
	1 ₀₁ - 0 ₀₀	-	42064.1497	2.02	0.42
	1 ₁₁ - 0 ₀₀	-	49615.8607	2.38	4.38
	2 ₁₁ - 2 ₀₂	o	34477.1066	6.84	1.52
c-C ₃ D ₂	1 ₁₁ - 0 ₀₀	o	45358.8400	2.18	3.87
ARO 12m					
c-C ₃ H ₂	2 ₂₀ - 1 ₁₁	p	150436.5547	9.71	53.57
	4 ₀₄ - 3 ₁₃	p	150820.6650	19.31	163.64
	3 ₁₂ - 2 ₂₁	o	145089.6055	16.05	135.62
	4 ₁₄ - 3 ₀₃	o	150851.9080	19.31	163.77
	4 ₁₄ - 3 ₀₃	-	136370.9100	17.39	137.24
c-C ₃ HD	2 ₂₀ - 1 ₁₁	-	137454.4640	8.98	102.75
IRAM 30m					
c-C ₃ HD	3 ₀₃ - 2 ₀₂	-	106811.0901	10.85	7.87
c-C ₃ D ₂	3 ₀₃ - 2 ₁₂	p	94371.3538	9.85	33.73

Notes. The spectral information for the molecular transitions including the frequency, the upper energy, (E_{up}), and the Einstein coefficient, (A_{ij}), was taken from The Cologne Database for Molecular Spectroscopy (CDMS)^a (c-C₃H₂: [Bogey et al. 1986](#); [Vrtilek et al. 1987](#); [Lovas et al. 1992](#); [Spezzano et al. 2012](#), c-C₃HD: [Bogey et al. 1986](#); [Spezzano et al. 2012](#), c-C₃D₂: [Spezzano et al. 2012](#)). For each transition an o, p or - indicates whether the transition is ortho, para or non-applicable.

^a <https://cdms.astro.uni-koeln.de>

Table 3. Number of detected transitions per isotopologue and core.

Core Number	c-C ₃ H ₂	c-C ₃ HD	c-C ₃ D ₂
264	6	4	0
317	6	4	0
321	6	4	1
326	6	5	0
413	6	5	1
504	6	5	2
615	6	4	0
627	6	4	1
709	6	4	0
715	6	4	1
746	6	4	1
752	0	0	0
768	6	4	0
799	6	4	1
800	6	5	2
L1448	-*	1	1

Notes. A transition is considered to be detected when its peak temperature $\geq 3\sigma$. * L1448 was not targeted for c-C₃H₂.

ortho and para. These different states arise from the orientation of the two protons' spin directions. Ortho corresponds to nuclear wavefunctions that have a total spin $I_{\text{tot}} = 1$ and are symmetric to interchange of the protons. Para nuclear wavefunctions have $I_{\text{tot}} = 0$ and are anti-symmetric to interchange of the protons. The intercon-

version between ortho and para is low, due to the weakness of the nuclear magnetic interaction, which makes it possible to treat ortho and para states as two different molecules.

The c-C₃H₂ molecule has two equivalent protons, which consequentially, results in a separation of ortho and para states. The spin of the hydrogen atom is $\pm 1/2$. If we take into account the relation between the spin of the atom and the total spin of the molecule, $I_{\text{tot}} = |I_1 - I_2|, \dots, I_1 + I_2$, where $I_{1,2}$ are the nuclear spin of each atom, the total nuclear spin of c-C₃H₂ can be either 0 or 1. Knowing that the number of individual states is given by $2I_{\text{tot}} + 1$, then for $I_{\text{tot}} = 0$ we get 1 state and for $I_{\text{tot}} = 1$ we get 3 states. In this case $I_{\text{tot}} = 0$ correspond to the para states and $I_{\text{tot}} = 1$ correspond to the ortho states. Then, statistically, the ortho-to-para ratio of c-C₃H₂ is 3. Due to its symmetry, for c-C₃H₂, the states that have quantum numbers K_a and K_c such that $K_a + K_c = \text{odd}$ value will be ortho and the states that have $K_a + K_c = \text{even}$ will be para. This is why for example the 3₂₁ - 3₁₂ transition (see Table 2) is an ortho transition. Nevertheless, the ortho-to-para ratio can be non-statistical due to the physical conditions of the environment. For example, the H₂ otp ratio is seen to be lower than 3 in prestellar cores (< 0.01 ; [Pagani et al. 2009](#); [Dislaire et al. 2012](#)) due to the low temperatures present. The protons in the c-C₃HD molecule are not equivalent and thus, do not present ortho and para substates. On the other hand the protons in c-C₃D₂ are equivalent and this molecule will show separate ortho and para states. The spin in the case of deuterium is 1. Following the same reasoning as for c-C₃H₂, the $I_{\text{tot}} = 0, 1, 2$, with a number of

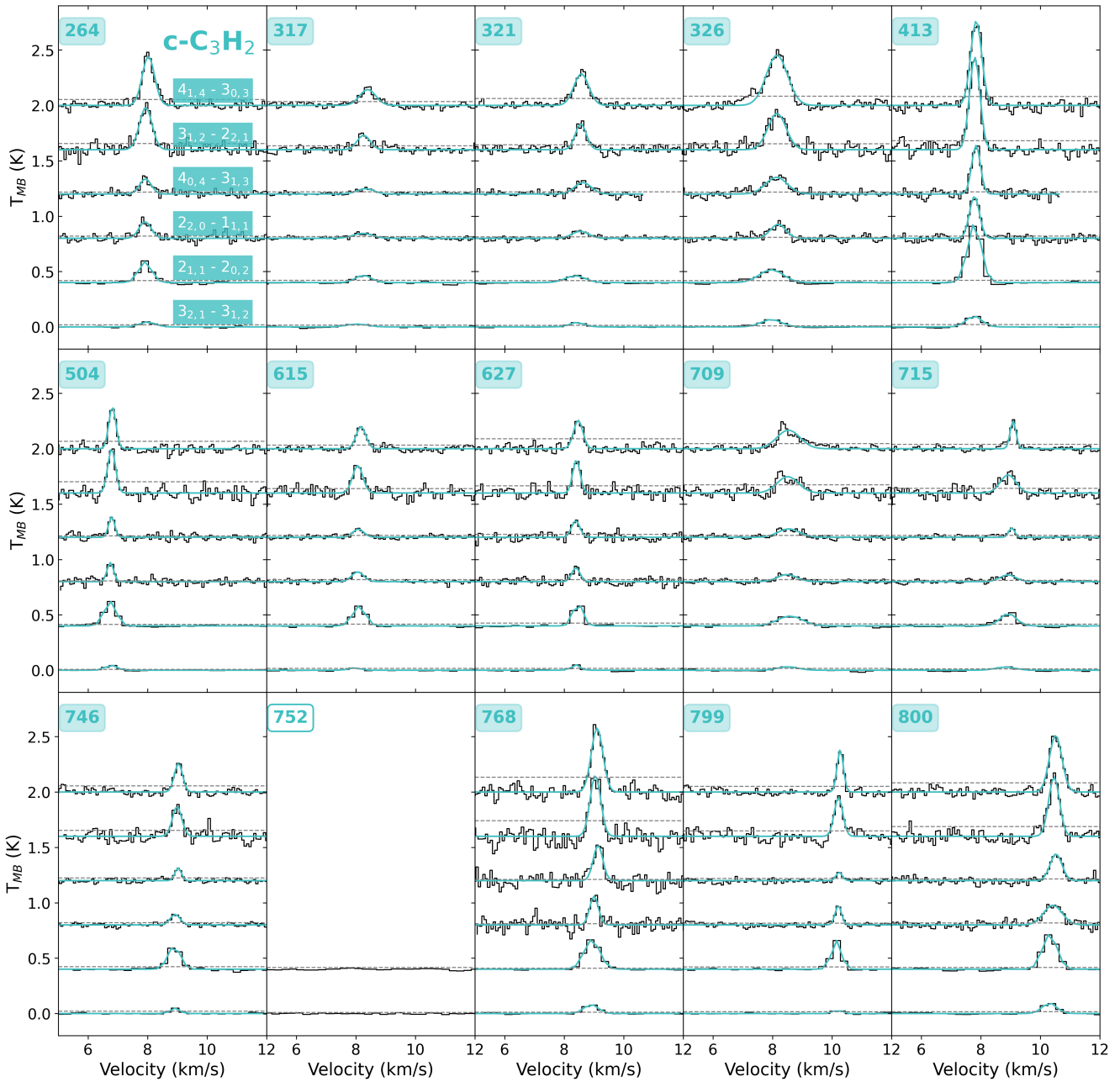


Fig. 2. Observed spectra of the c-C₃H₂ transitions organised by core number. All of the transitions for the same core are plotted in the same subplot with vertical offsets for clarity. The Gaussian fit from pyspeckit are overplotted with a blue line. The spectra without a Gaussian fit indicate a non-detection. Core number labels with a colour background indicate c-C₃H₂ has been detected towards the source. Lastly, horizontal gray dashed lines indicates 3σ levels.

states equal to 1, 3 and 5, respectively. In the case of c-C₃D₂ $I_{\text{tot}} = 0$ and 2, accounting for 6 symmetric nuclear wavefunctions, are ortho, and $I_{\text{tot}} = 1$, accounting for 3 anti-symmetric wavefunctions, are para. Thus, the statistical ratio of c-C₃D₂ is 2. Due to the symmetry of c-C₃D₂, the states that have $K_a + K_c = \text{odd}$ value will be para and the ones that have $K_a + K_c = \text{even}$ will be ortho. Notice that the $K_a + K_c$ rule is opposite for the c-C₃H₂ and c-C₃D₂ molecules. As ortho- and para-c-C₃D₂ were not detected both towards the same cores, its ortho-to-para ratio could not be studied.

Three ortho and three para-c-C₃H₂ transitions have been detected towards all of the cores (except for Per752 and L1448) which allows us to obtain otp ratios for 14

cores. The ortho-c-C₃H₂ column density is divided by the para-c-C₃H₂ column density. The otp ratios are listed in Table 5. In Figure 7 the otp ratios and its errors are plotted for the different cores in blue. The median value of 3.5 ± 0.4 is plotted with a gray dashed line and with a gray band, respectively. The median uncertainty is calculated with the bootstrap method, which is a statistical resampling technique used to estimate the uncertainty of measured parameters.

All of the cores present a statistical otp ratio of 3 within errors except for core Per799 which has a higher otp ratio: 4.7 ± 1.6 .

The c-C₃H₂ otp ratio has been plotted vs the volume density and kinetic temperature of the cores with the

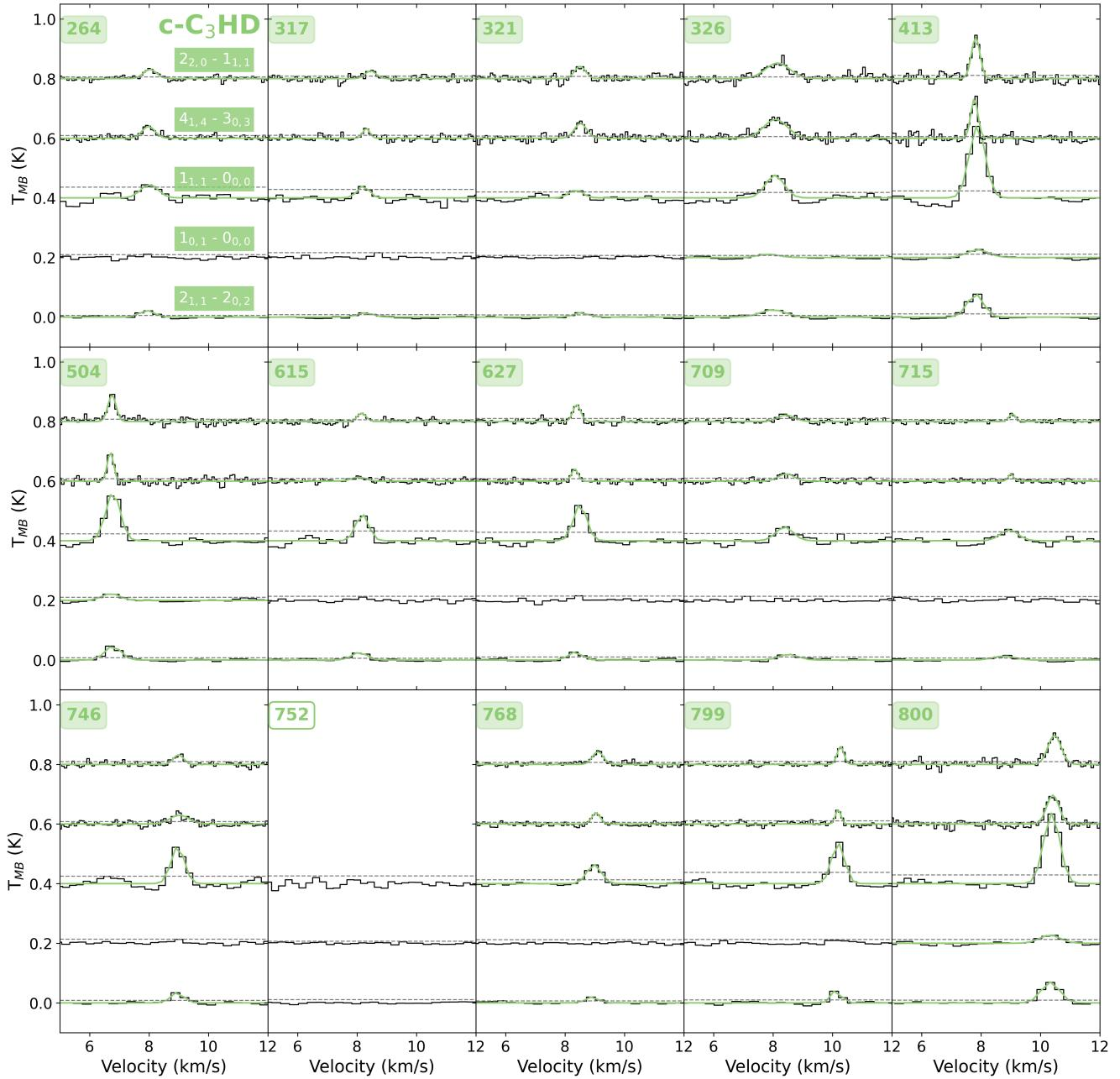


Fig. 3. Same as Figure 2 for c-C₃HD. Here the Gaussian fits and labels are plotted with the colour green.

aim of finding possible correlations (Figure 8, right and left panels respectively). No correlations have been found for the otp ratio either with n_{H_2} nor with T_{kin} ($r = -0.20$ and -0.34 , respectively). Also, no trends have been found for the otp ratio regarding the cloud subregion.

4.2. c-C₃HD

For c-C₃HD a total of five lines were targeted, three at lower frequencies with the Yebes 40m telescope: $2_{11} - 2_{02}$, $1_{01} - 0_{00}$ and $1_{11} - 0_{00}$; one at intermediate frequencies with the IRAM 30m telescope: $3_{03} - 2_{02}$; and two at higher frequencies with the ARO 12 m telescope: $4_{14} - 3_{03}$ and $2_{20} - 1_{11}$. The observed lines with their Gaussian fits from pyspeckit are plotted in Figures 3 and 5 for source L1448.

c-C₃HD is detected towards 15/16 cores ($\sim 94\%$). The only core where c-C₃HD was not detected is Per752. The column density values can be found on Table 4, except for Per752 for which we give upper limits. The Per752 core was exclusively observed with the Yebes 40m data, and thus, the upper limit column density in this case is estimated just with the $2_{11} - 2_{02}$, $1_{01} - 0_{00}$ and $1_{11} - 0_{00}$ transitions. A line width of 0.5 km s^{-1} was assumed. For cores Per264, Per317, Per321, Per326, Per709, Per715 and Per800, transition $1_{11} - 0_{00}$ is badly fit by RADEX, giving unexpected high T_{ex} values. Thus, this transition is excluded from the fit towards these cores. The c-C₃HD column density values found range from $2.0 \pm 0.3 \times 10^{11} \text{ cm}^2$ (Per317) to $1.9 \pm 0.2 \times 10^{12} \text{ cm}^2$ (Per800), with a weighted average of $4.0 \pm 0.1 \times 10^{11} \text{ cm}^2$ (not taking into account the upper limit of Per752).

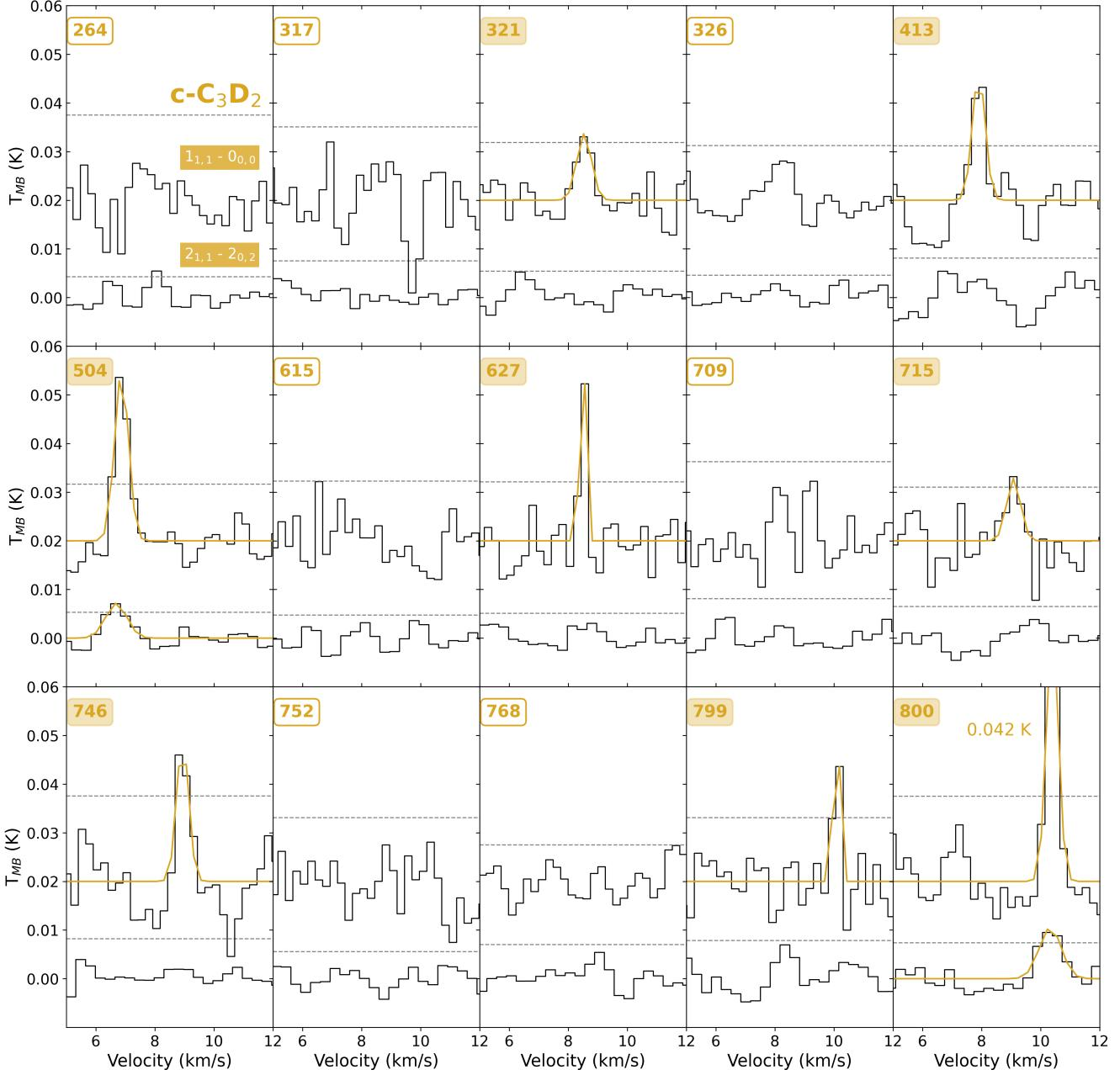


Fig. 4. Same as Figure 2 for c-C₃D₂. Here the Gaussian fits and labels are plotted with the colour orange.

The median of T_{ex} for $2_{1,1} - 2_{0,2}$ is 8.4 K, for $1_{0,1} - 0_{0,0}$ is 5.6 K, for $1_{1,1} - 0_{0,0}$ is 12.8 K, for $4_{1,4} - 3_{0,3}$ is 4.9 K and for $2_{2,0} - 1_{1,1}$ is 4.6 K. The optical depth (τ) does not change much within transitions with a median of 0.02.

4.3. c-C₃D₂

For c-C₃D₂ a total of three lines were targeted, two at lower frequencies with the Yebes 40m telescope: $2_{11} - 2_{02}$ (o) and $1_{11} - 0_{00}$ (o); and one at intermediate frequencies with the IRAM 30m telescope: $3_{03} - 2_{12}$ (p). The observed lines with their Gaussian fits from pyspeckit are plotted in Figures 4 and 5, for source L1448.

c-C₃D₂ was detected towards 9/16 cores ($\sim 56\%$). The cores where c-C₃D₂ is not detected are Per264,

Per317, Per326, Per615, Per709, Per752 and Per768. There is not a perfect correlation between the cores with the highest c-C₃HD column densities and c-C₃D₂ detections. For example, c-C₃D₂ has not been detected towards Per326, one of the cores with the highest c-C₃HD column densities.

All of the detected c-C₃D₂ transitions are ortho except for one para transition detected towards L1448. As we do not have both ortho- and para-c-C₃D₂ for the same cores we assume a statistical otp ratio of 2 (see Section 4.1.1) to calculate the total c-C₃D₂ column densities. The total-c-C₃D₂ column densities can be found on Table 4, except for Per264, Per317, Per326, Per615, Per709, Per752 and Per768 for which we give upper limits. For these cores c-C₃D₂ was exclusively targeted with the Yebes 40m data, and thus, the upper limit column den-

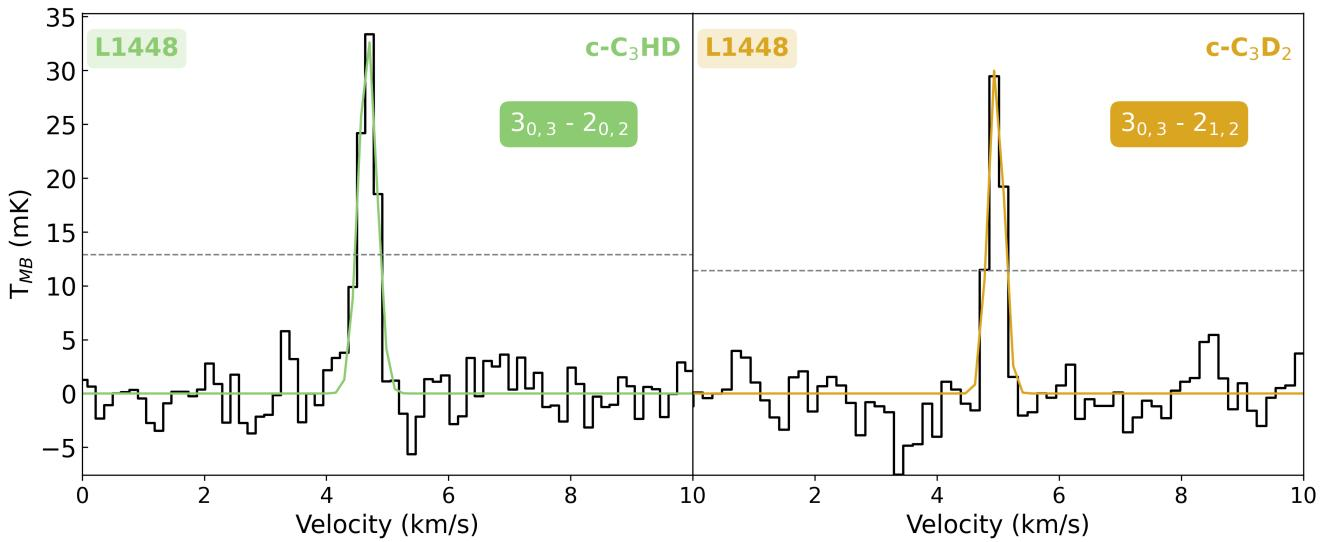


Fig. 5. Observed spectra and the Gaussian fit from pyspeckit of c-C₃HD, in green, and c-C₃D₂, in orange. Horizontal gray dashed lines indicates 3σ levels.

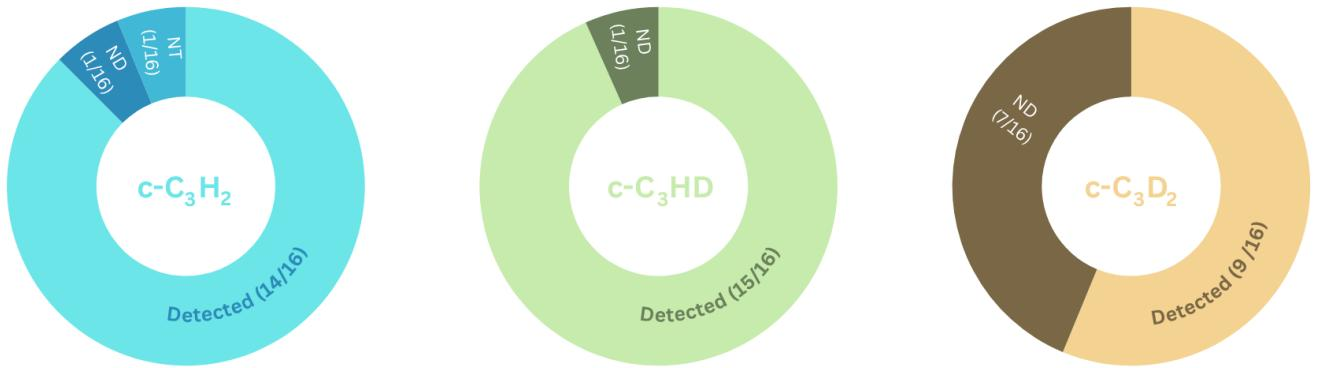


Fig. 6. Detection statistics of c-C₃H₂, in blue, c-C₃HD, in green, and c-C₃D₂, in orange. The pie chart shows three categories: Detected, Not-detected (ND), and Not-targeted (NT). c-C₃H₂ and c-C₃HD were not targeted towards one of the cores, while C₃D₂ was targeted towards all of them.

sity in this case is estimated with the $2_{1,1} - 2_{0,2}$ and $1_{1,1} - 0_{0,0}$ transitions. As these are ortho transitions the total column density upper limit was calculated assuming an ortho-to-para ratio of 2. As for the other molecules, a line width of 0.5 km s⁻¹ was assumed. RADEX is not able to find a solution for the para $3_{0,3} - 2_{1,2}$ transition observed towards L1448. As there is just one c-C₃D₂ transition targeted towards L1448, we calculate the column density of the molecule by assuming an excitation temperature of 5 K, as RADEX found a T_{ex} of ~ 6 K for c-C₃HD towards the same source. The c-C₃D₂ column density values found range from $5.8 \pm 1.6 \times 10^{10}$ (Per715) to $1.6 \pm 0.2 \times 10^{11}$ (Per800), with a weighted average of $9.9 \pm 0.7 \times 10^{10}$ (not taking into account the upper limits of non detections).

The excitation temperature (T_{ex}) of c-C₃D₂ transitions tends to be higher than that of the other isotopologues. The T_{ex} value derived for the $1_{1,1} - 0_{0,0}$ transition is in average larger than for $2_{1,1} - 2_{0,2}$, with medians 13.6 and 8.2 K. The median τ for $1_{1,1} - 0_{0,0}$ of all cores is 0.004 and for $2_{1,1} - 2_{0,2}$ is 0.002.

4.4. c-C₃H₂ Deuteration Ratios

The c-C₃HD/c-C₃H₂ (D/H) ratio has been obtained towards all of the cores except towards Per752, where neither c-C₃H₂ nor c-C₃HD were detected, and L1448, as we do not have data covering c-C₃H₂ transitions. The c-C₃D₂/c-C₃HD (D₂/D) ratio is obtained towards 9 cores including Per321, Per413, Per504, Per627, Per715, Per746, Per799, Per800 and L1448 (see Table 4).

Two types of deuteration ratios are given, the direct ones where the column densities of the isotopologues are divided, and the corrected ones, which take into account statistical corrections. We use the statistical correction formula taken from Appendix C of [Drozdovskaya et al. \(2022\)](#). To calculate the (D/H)_{c-C₃H₂} from the c-C₃HD/c-C₃H₂ ratio we employ the following equation,

$$\frac{XH_{n-i}D_i}{XH_n} = \binom{n}{i} \left(\frac{D}{H}\right)_{XH_n}^i \quad (2)$$

where n are the equivalent H atom positions and i is the number of deuteriums. If we substitute and solve for the

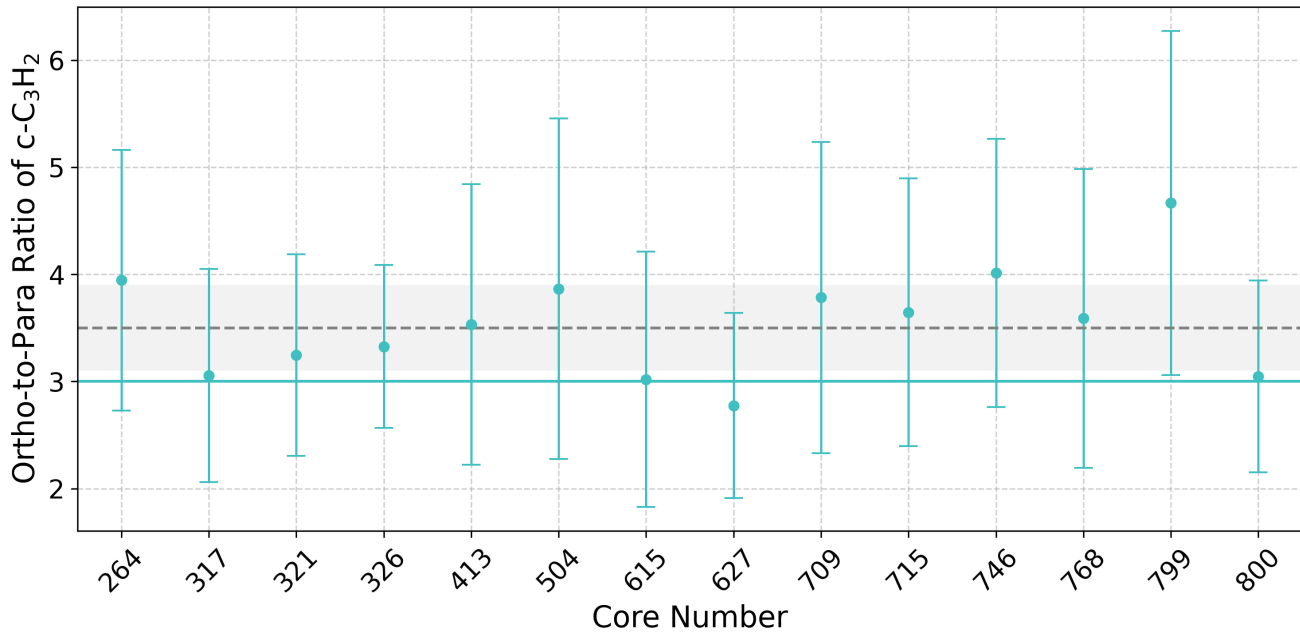


Fig. 7. c-C₃H₂ ortho-to-para ratios and their uncertainties are plotted for each core in blue. The median otp value as well as its standard deviation for all of the cores (3.5 ± 0.4) are plotted with a gray horizontal dashed line and gray band, respectively. The statistical value of 3 is marked by a horizontal solid blue line.

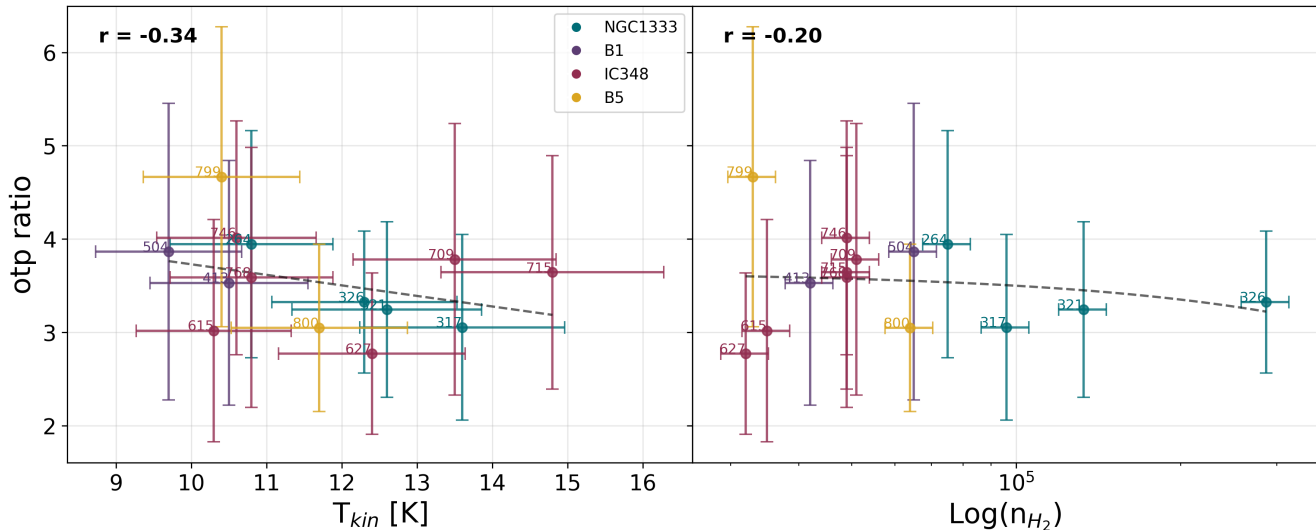


Fig. 8. Ortho-to-para ratios plotted versus the kinetic temperature, left panel, and volume density, right panel, of the cores. The cores belonging to different regions within the Perseus Molecular Cloud are plotted with different colours (NGC1333 in teal, B1 in purple, IC348 in red and B5 in yellow). The x axis in the right panel is plotted in logarithmic scale for clarity. The gray dashed line indicates the linear correlation trend between the two variables. On the top left corner the Pearson correlation coefficient is displayed.

statistically-corrected ratio $(D/H)_{c-C_3H_2}$ we get,

$$\left(\frac{D}{H}\right)_{c-C_3H_2} = \frac{1}{2} \times \frac{c - C_3HD}{c - C_3H_2} \quad (3)$$

which indicates that the ratio of the c-C₃HD/c-C₃H₂ column densities needs to be multiplied by 1/2. Using the formula,

$$\frac{XH_{n-i}D_i}{XH_{n-j}D_j} = \frac{\binom{n}{i}}{\binom{n}{j}} \left(\frac{D}{H}\right)_{XH_{n-j}D_j}^{i-j} \quad (4)$$

where j is the number of deuteriums in the other isotope, we see that to obtain $(D/H)_{c-C_3HD}$ we need to multiply c-C₃D₂/c-C₃HD by a factor of 2.

With the aim of comparing these deuteration ratios with other molecules, we will use the statistically corrected values in discussion.

The c-C₃H₂ D/H ratios range from 0.5 to 9.2% with a median value of 1.5 ± 0.2 %. The core with the lowest D/H ratio is Per768 and the one with the highest is Per326. The c-C₃H₂ D₂/D ratios range from 9.0 to 55.2% with a median value of 25.9 ± 4.3 %. The core

with the lowest detected ratio is Per413 and the one with the highest, Per715.

To explore the possible correlations of deuteration with the physical properties of cores, the D/H and D₂/D ratios are plotted against the n_{H_2} and T_{kin} (see Figures 9 and 10, respectively). A correlation is found between the D/H ratio and the n_{H_2} of the cores, with a correlation coefficient of 0.94, indicating that the D/H ratio is indeed higher for denser cores (Figure 9, right panel). On the other hand, there is no correlation found for D/H vs T_{kin} ($r = 0.12$, Figure 9, left panel). Contrary to the D/H ratio, D₂/D presents no correlation with n_{H_2} ($r = -0.24$, Figure 10, right panel), but it shows a correlation with T_{kin} ($r = 0.65$, 10, left panel). Finally, plotting D/H against D₂/D does not give a strong correlation ($r = -0.39$, Figure 11).

5. Discussion

c-C₃H₂ has been detected towards the entire subset of cores, except Per752, for which an upper column density limit is given. Per752 is the core with the lowest volume density of the cores studied in this paper. This, in combination with the slightly larger T_{kin} , could result in not sufficient emission to be detected with the sensitivity of the current observations. However, other molecules, including COMs, e.g. CH₃OH, CH₃CHO, CH₃CN, t-HCOOH and H₂CCO have been detected towards this core (Scibelli et al. 2024). Thus, the c-C₃H₂, non detection towards Per752 appears to be directly related to this specific molecule instead of this core being generally chemically poor. In Pokorny-Yadav et. al. (in prep.), carbon chains were specifically surveyed in the same starless and prestellar core selection towards the Perseus Molecular Cloud. In the above mentioned study, Per752 presents almost no carbon chains detection, which is in agreement with the non detection of c-C₃H₂ in this study. Thus, Per752 is particularly poor in carbon chain molecules, suggesting that the physical characteristics and environment of this core are favourable for the production of COMs but not of carbon chains (see Pokorny-Yadav et. al. (in prep.)).

5.1. c-C₃H₂ otp Ratio

The statistical ortho to para ratio of c-C₃H₂ is 3 (see Section 4.1.1). However, this ratio can deviate from the statistical value due to different factors such as the initial non-statistical otp ratio of the reactants and interconversion ratio reactions (Furuya et al. 2015; Lupi et al. 2021).

Observational studies have explored the otp ratio of c-C₃H₂ towards TMC-1 (Madden et al. 1989; Takakuwa et al. 2001; Morisawa et al. 2006) and L1527 (Takakuwa et al. 2001). These studies showed that the otp ratio towards prestellar cores can deviate from the statistical value. Morisawa et al. (2006) find a direct correlation between the core's evolutionary stage, as measured with the NH₃/CCS abundance ratio, and its otp ratio, with lower otp ratios observed towards younger cores. However, the gas-phase chemical modelling of the otp ratio of c-C₃H₂ done in Park et al. 2005, which includes ortho-to-para interconversion reactions, is not able to reproduce the observed ratios in Morisawa et al. (2006). Nevertheless,

they claim observational uncertainties or the incompleteness of the reaction network could have impacted the results. Thus, the correlation between the otp ratio and the evolutionary stage of the core is not confirmed.

The otp ratio of c-C₃H₂ studies are limited to TMC-1 and L1527. In this study, we expand these observations to the Perseus Molecular Cloud to understand whether the deviation of the otp ratio also happens in other starless and prestellar cores.

As seen in Section 4.1.1, all of the cores except for one have a statistical otp ratio of 3 within uncertainty. The median otp ratio of the core sample is 3.5 ± 0.4 . Due to the limited sensitivity of the observations, the uncertainties or the otp ratios are large, and possible non-statistical ratios towards other cores are not seen. Due to the possibility of c-C₃H₂ otp ratios deviating from its statistical value of 3, as seen in previous works (Madden et al. 1989; Takakuwa et al. 2001; Morisawa et al. 2006) and as hinted in this one, calculating total c-C₃H₂ column densities from either only the ortho- or para-c-C₃H₂ column densities by assuming an otp ratio of 3 is not always safe. If possible, both ortho- and para-c-C₃H₂ transitions should be observed to get an accurate total c-C₃H₂ column density. Plotting otp ratios against n_{H_2} and T_{kin} does not give any trends (with correlation coefficients of -0.20 and -0.34 in Figure 8, right and left panels, respectively). If we assume a direct relationship between the core volume density and its evolutionary stage, contrarily to Morisawa et al. (2006), we do not see a trend of increasing otp ratios with evolutionary stage (Figure 8). The absence of a trend could be due to the uncertainties related to the derived otp ratios. However, the c-C₃H₂ otp ratios may also be determined by many more variables other than core evolutionary stage, making the c-C₃H₂ otp ratio not a reliable proxy for core evolutionary stage.

5.2. c-C₃H₂ Deuteration

c-C₃HD, as its main isotopologue, is detected towards all of the cores in the sample except Per752. On the other hand, c-C₃D₂ is detected towards a smaller number of cores (Per321, Per413, Per504, Per627, Per715, Per746, Per799 and Per800). To test whether the cores where c-C₃D₂ is detected could be the cores with highest D/H ratios, we plotted the D/H vs the D₂/D ratios, but no clear trend was seen ($r = -0.39$, Figure 11).

Plotting the c-C₃H₂ D/H and D₂/D ratios against the volume density (n_{H_2}) of the cores shows a direct correlation between D/H and n_{H_2} ($r = 0.94$, Figure 9, right panel) but no correlation for D₂/D and n_{H_2} ($r = -0.24$, Figure 10, right panel). D/H scaling with n_{H_2} agrees with the idea that the more evolved cores, which are denser, are the ones that present higher deuteration ratios. Nevertheless, in Chantzos et al. (2018) they do not find a correlation between the D/H ratio and the central column densities of Taurus starless and prestellar cores. If Per326 is removed from the Perseus correlation then a Pearson correlation coefficient of 0.76 is obtained. If both the Per326 and Per321 cores are removed then a Pearson correlation coefficient of 0.42 is obtained. If instead the Spearman rank correlation coefficient (ρ), which measures the strength and direction of a monotonic relationship between two variables, is used, the value 0.64 is

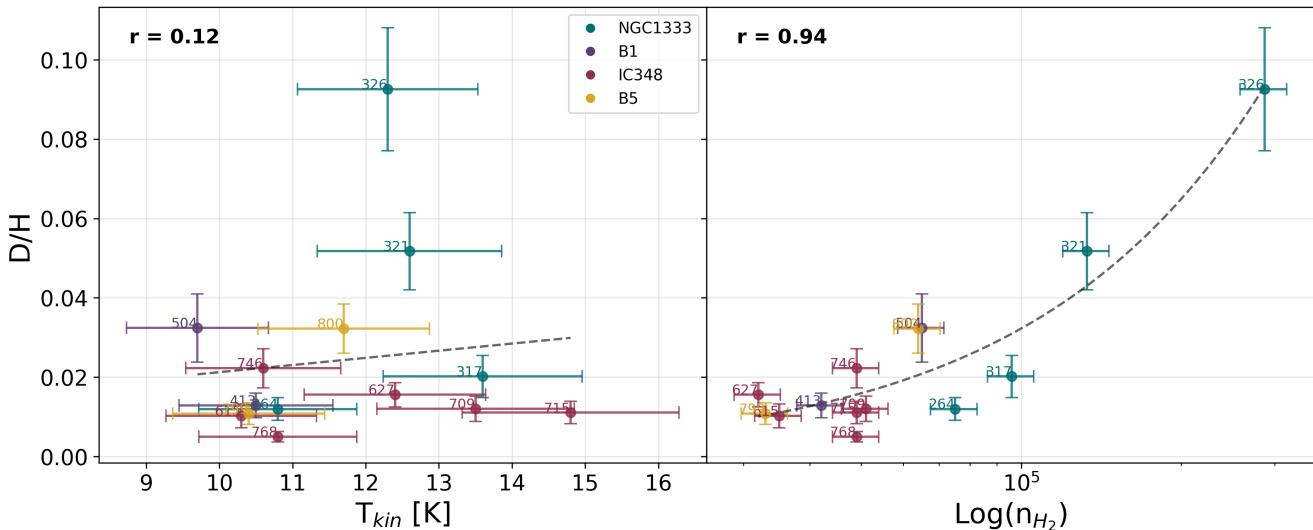


Fig. 9. D/H ratios plotted versus the kinetic temperature, left panel, and volume density, right panel, of the cores. The cores belonging to different regions within the Perseus Molecular Cloud are plotted with different colours. The x axis in the volume density plot is plotted in logarithmic scale for clarity. The gray dashed line indicates the linear correlation trend between the two variables. The Pearson correlation coefficient is displayed on the top left.

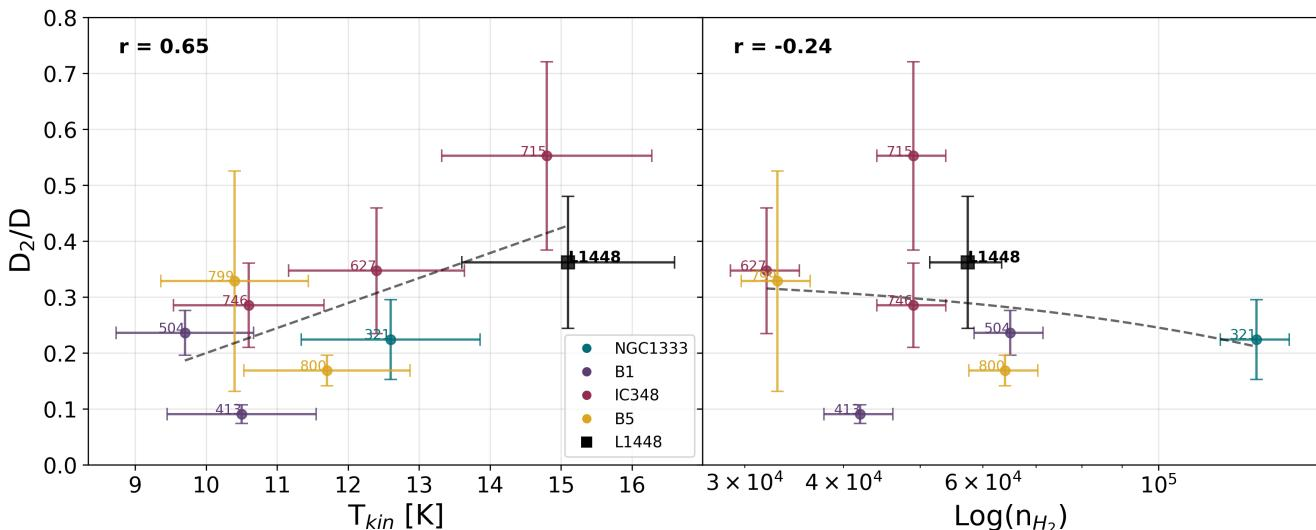


Fig. 10. D₂/D ratios plotted versus the kinetic temperature, left panel, and volume density, right panel, of the cores. The cores belonging to different regions within the Perseus Molecular Cloud are plotted with different colours. The x axis in the volume density plot is plotted in logarithmic scale for clarity. The gray dashed line indicates the linear correlation trend between the two variables. The Pearson correlation coefficient is displayed on the top left.

obtained. The correlation found between D/H and n_{H_2} seem to be governed by these two more massive cores. On the other hand, the D₂/D ratio does not appear to follow this trend. This can be due to the fact that the detection sample spans a narrower range in volume densities compared to the D/H ratio. Nevertheless, the D₂/D ratio not correlating with volume density may point to the independence of the second deuteration of c-C₃H₂ from density, unlike D/H ratio.

The c-C₃H₂ D/H and D₂/D ratios were also plotted against the kinetic temperature (T_{kin}) of the cores, as it is known that low temperatures enhance deuterium fractionation (Figures 9 and 10, respectively). No clear trend is observed for the D/H ratio, but there is a positive correlation for the D₂/D one. The lack of correlation

between D/H and T_{kin} may be due to the fact that T_{kin} does not necessarily represent the temperature of the inner part of the core where deuterium fractionation is enhanced. This is supported by the lack of correlation ($r = 0.15$) between n_{H_2} and T_{kin} (Figure 12), which would be expected if T_{kin} represented the temperature at the centre of the core which would decrease with increasing n_{H_2} . The positive correlation of D₂/D with T_{kin} could be explained if the second deuteration happened, at least partly, in the gas phase through slightly endothermic reactions, as for example with CH₂D⁺.

c-C₃H₂ is thought to be formed in the gas phase mainly by the electron recombination of c-C₃H₃⁺ (Loison et al. 2017). The formation of its deuterated isotopologues is thought to occur through the deuteration

Table 4. Obtained column densities, D/H and D₂/D ratios.

Core Number	c-C ₃ H ₂	c-C ₃ HD	c-C ₃ D ₂	D/H	D/H _{corr}	D ₂ /D	D ₂ /D _{corr}
264	$1.8 \pm 0.4 \times 10^{13}$	$4.4 \pm 0.6 \times 10^{11}$	$\leq 5.7 \pm 1.4 \times 10^{10}$	0.024(0.006)	0.012(0.003)	-	-
317	$5.0 \pm 1.0 \times 10^{12}$	$2.0 \pm 0.3 \times 10^{11}$	$\leq 6.6 \pm 1.6 \times 10^{10}$	0.040(0.010)	0.020(0.005)	-	-
321	$6.3 \pm 1.1 \times 10^{12}$	$6.6 \pm 0.5 \times 10^{11}$	$7.4 \pm 2.3 \times 10^{10}$	0.103(0.019)	0.052(0.010)	0.112(0.036)	0.224(0.071)
326	$8.0 \pm 1.1 \times 10^{12}$	$1.5 \pm 0.1 \times 10^{12}$	$\leq 5.4 \pm 1.4 \times 10^{10}$	0.185(0.031)	0.092(0.015)	-	-
413	$8.1 \pm 1.8 \times 10^{13}$	$2.1 \pm 0.1 \times 10^{12}$	$9.5 \pm 1.6 \times 10^{10}$	0.026(0.006)	0.013(0.003)	0.045(0.008)	0.090(0.017)
504	$1.8 \pm 0.4 \times 10^{13}$	$1.1 \pm 0.1 \times 10^{12}$	$1.3 \pm 0.2 \times 10^{11}$	0.065(0.017)	0.032(0.009)	0.118(0.020)	0.236(0.040)
615	$2.1 \pm 0.5 \times 10^{13}$	$4.3 \pm 0.6 \times 10^{11}$	$\leq 5.1 \pm 1.2 \times 10^{10}$	0.020(0.006)	0.010(0.003)	-	-
627	$1.7 \pm 0.3 \times 10^{13}$	$5.4 \pm 0.5 \times 10^{11}$	$9.3 \pm 2.9 \times 10^{10}$	0.031(0.006)	0.016(0.003)	0.173(0.056)	0.347(0.112)
709	$1.6 \pm 0.4 \times 10^{13}$	$4.0 \pm 0.6 \times 10^{11}$	$\leq 4.6 \pm 1.7 \times 10^{10}$	0.024(0.006)	0.012(0.003)	-	-
715	$9.4 \pm 2.1 \times 10^{12}$	$2.1 \pm 0.2 \times 10^{11}$	$5.8 \pm 1.6 \times 10^{10}$	0.022(0.006)	0.011(0.003)	0.276(0.084)	0.552(0.168)
746	$1.6 \pm 0.3 \times 10^{13}$	$7.2 \pm 0.9 \times 10^{11}$	$1.0 \pm 0.2 \times 10^{11}$	0.044(0.010)	0.022(0.005)	0.142(0.038)	0.285(0.075)
752	$\leq 4.2 \pm 1.7 \times 10^{12}$	$\leq 3.1 \pm 0.8 \times 10^{11}$	$\leq 5.6 \pm 1.4 \times 10^{10}$	-	-	-	-
768	$4.3 \pm 1.0 \times 10^{13}$	$4.2 \pm 0.5 \times 10^{11}$	$\leq 5.0 \pm 1.3 \times 10^{10}$	0.010(0.003)	0.005(0.001)	-	-
799	$2.8 \pm 0.6 \times 10^{13}$	$6.0 \pm 0.6 \times 10^{11}$	$9.8 \pm 5.8 \times 10^{10}$	0.022(0.005)	0.011(0.003)	0.164(0.098)	0.328(0.197)
800	$3.0 \pm 0.5 \times 10^{13}$	$1.9 \pm 0.2 \times 10^{12}$	$1.6 \pm 0.2 \times 10^{11}$	0.064(0.012)	0.032(0.006)	0.084(0.013)	0.169(0.027)
L1448	-	$7.8 \pm 1.9 \times 10^{11}$	$1.4 \pm 0.3 \times 10^{11}$	-	-	0.181(0.059)	0.362(0.118)

Notes. The “-” symbol is used to indicate towards the L1448 the c-C₃H₂ molecule was not targeted and also that some D/H and D₂/D have not been able to be calculated due to one or more isotopologues not being detected. The D/H ratios have been corrected by multiplying by two and the D₂/D by dividing by two. The upper limits correspond to the 3 σ level.

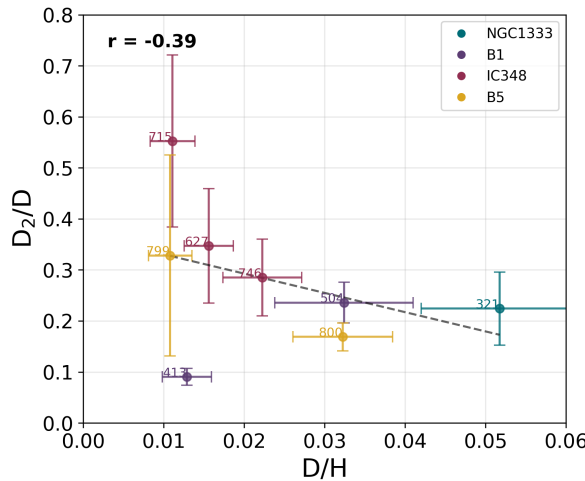


Fig. 11. D₂/D ratios plotted versus the D/H ratios. The cores belonging to different regions within the Perseus Molecular Cloud are plotted with different colours. The gray dashed line indicates the correlation trend between the two variables. On the top left corner the correlation coefficient is displayed.

of its main isotopologue with H₂D⁺, D₂H⁺ and D₃⁺, followed by an electron recombination (Spezzano et al. 2013). In this scenario, the deuteration fraction increases with time, owing to the cores getting lower temperatures at their centre due to their increasing densities, and the H₂D⁺ molecule being formed more efficiently. This is seen in our results where the D/H ratio directly correlates with the core volume density. On the other hand we see that the D₂/D ratio does not correlate with n_{H_2} , but positively correlates with T_{kin} . This seems to indicate the second deuteration of c-C₃H₂ is enhanced by a slightly endothermic reaction. Then when T_{kin} is higher it favours these type of reactions resulting into higher D₂/D ratios. Reaction with CH₂D⁺ is thought to become the main deuteration path at warm temperatures ($\gtrsim 30$ K), as the formation mechanism of CH₂D⁺, is slightly more

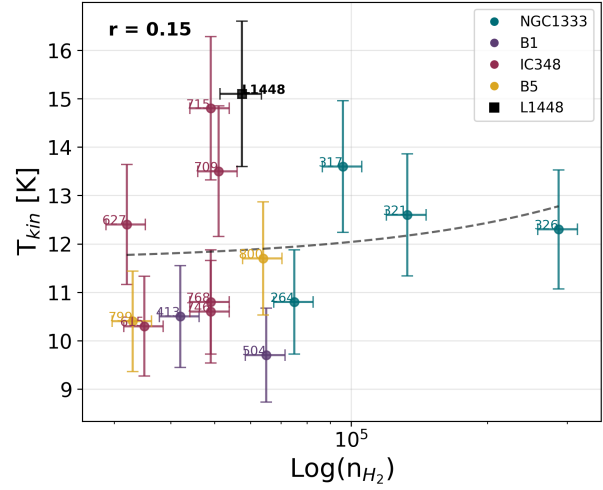


Fig. 12. Kinetic temperatures of clouds plotted against their volume densities. The x axis is plotted in logarithmic scale for clarity. The cores belonging to different regions within the Perseus Molecular Cloud are plotted with different colours. The gray dashed line indicates the correlation trend between the two variables. On the top right corner the correlation coefficient is displayed.

endothermic than the formation mechanism of H₂D⁺. It is possible then, that at the “warmer” external layers of the cores, traced by T_{kin} , deuteration reactions with CH₂D⁺ start being relevant. There is also the possibility that other slightly endothermic reactions, are responsible for the higher D₂/D ratios observed towards warmer cores in the Perseus Molecular Cloud. Follow-up work would be needed to assess this scenario in greater detail.

The larger D₂/D ratio compared to the D/H one indicates that the second deuteration, from c-C₃HD to c-C₃D₂, is more effective than the first deuteration from c-C₃H₂ to c-C₃HD. This phenomenon, where the second deuteration is more effective than the first one, has

Table 5. Obtained c-C₃H₂ ortho-to-para ratios along the studied cores.

Core Number	otp ratio
264	3.9±1.2
317	3.0±1.0
321	3.2±0.9
326	3.3±0.8
413	3.5±1.3
504	3.9±1.6
615	3.0±1.2
627	2.8±0.9
709	3.8±1.4
715	3.6±1.2
746	4.0±1.2
768	3.6±1.4
799	4.7±1.6
800	3.0±0.9

been observed in other molecules. For example, observations towards the prestellar core L1544 show that D₂CS is relatively more abundant than HDCS, indicating enhanced second deuteration of thioformaldehyde (Spezzano et al. 2022). Studies of formaldehyde towards the protostellar system IRAS 16293-2422 reveal a higher D₂CO/HDCO ratio than HDCO/H₂CO (Jørgensen et al. 2018); similarly, the amidogen radical in the same source exhibits unexpectedly high ND₂/NHD ratios, suggesting efficient multiple deuteration during prolonged cold prestellar phases (Melosso et al. 2020). This trend has also been observed for some COMs in IRAS 16293-2422 and the neighbouring prestellar core IRAS 16293E (Scibelli et al. (2025), for D₂/D in methanol). COMs in IRAS 16293-2422 display an average D₂/D ratio of ∼20% which is generally four times higher than their D/H ratios (Manigand et al. 2020; Richard et al. 2021; Drozdovskaya et al. 2022; Ferrer Asensio et al. 2022). These results point at least to the partial inheritance of these molecules from the prestellar phase where the conditions favour deuterium fractionation. This is confirmed by the methanol D/H and D₂/D ratios derived from the prestellar core IRAS 16293E (Scibelli et al. 2025) which formed in the same environment as the protostellar system IRAS 16293-2422.

It needs to be taken into account that some c-C₃H₂ transitions are optically thick $\tau > 1$ towards some cores Per413, Per504, Per627, Per768, Per799 and Per800. This means some D/H ratios could be enhanced as the column density of c-C₃H₂ would be underestimated. Nevertheless, these cores are not the densest cores that seem to be dominating the trend.

In Pokorny-Yadav et. al. (in prep.) they have studied the deuteration of HC₃N across the same group of Perseus starless and prestellar cores, finding a D/H ratio ranging between 1.8% (Per326) and 12.4% (Per321), with a median of 6.4%. In the case of c-C₃H₂ the core with the lowest D/H ratio is Per768 (0.5%), and the one with the highest is Per326 (9.2%), with a median of 1.5%. From these results we see that the formation of the singly-deuterated species for HC₃N is more efficient than the one for c-C₃H₂. Pokorny-Yadav et. al. (in prep.)

have found a correlation with the volume density of the cores, similarly as found for the D/H ratio of c-C₃H₂ in the present study (Figure 12 in Pokorny-Yadav et. al., in prep.). Nevertheless, in the case of HC₃N, Per326 and Per264 do not follow the trend, having lower D/H ratios. This behaviour is attributed to the local environment of cores Per326 and Per264, affecting the deuteration of HC₃N. These cores are located on the path of the outflows of the SVS13, IRAS 4A/B and IRAS 2A/B protostars. They suggest that shocks produced by the outflow impacts may release CO from dust grains, lowering the abundance of gas-phase deuteration molecules such as H₂D⁺. Contrarily to what is found for HC₃N, the c-C₃H₂ D/H ratio of cores Per264 and Per326 follow the positive correlation with n_{H_2} . This difference may come from the different chemical nature of the two molecules and their reactivity. Lastly, the HC₃N D/H median found towards the Perseus starless and prestellar cores in Pokorny-Yadav et. al. (in prep.) is consistent with D/H values measured in other prestellar and protostellar cores in Taurus and Serpens.

Moreover, the deuteration of H₂S, H₂CS and CH₃OH have also been studied towards some starless and prestellar cores in the Perseus Molecular Cloud. The deuteration of H₂S has been studied towards ten Perseus starless and prestellar cores, alongside cores in Taurus and Orion, in Rodríguez-Baras et al. (2023). HDS has been detected towards seven cores, while D₂S has been detected towards four cores. The D/H and D₂/D ratios derived towards the sample is higher than the ratios derived for c-C₃H₂ in this study. The deuteration of H₂CS is studied towards ten starless and prestellar cores in Perseus, additionally to other sources in Taurus and Orion. HDCS is detected towards seven cores, while D₂CS is detected towards five sources. The derived deuteration H₂CS ratios, appear higher than the ones found for c-C₃H₂ in this study. The higher deuteration ratios of H₂CS with respect to c-C₃H₂ was also observed towards the prestellar core L1544 (Spezzano et al. 2022). The D/H ratio of CH₃OH has been studied towards L1448 in Kulterer et al. (2025) giving a higher value also than the median D/H found in Perseus for c-C₃H₂. In general, previous studies have shown that H₂CS and H₂CO exhibit higher deuteration ratios towards starless and prestellar cores than c-C₃H₂, H₂S, H₂O and CH₃OH, which highlights the diversity in deuteration fractionation mechanisms for different molecules.

5.2.1. Comparison with the Taurus and Chamaeleon Molecular Clouds

The c-C₃H₂ D/H and D₂/D ratios have been derived towards other starless and prestellar cores in previous works. Most of these target cores in the Taurus Molecular Cloud except one work that derives the D/H value towards the prestellar core Cha-C2 in the Chamaeleon Molecular Cloud (Lis et al. 2025). Thus, a comparison of the deuteration of c-C₃H₂ in starless and prestellar cores between the Perseus, Taurus and Chamaeleon Molecular Clouds can be made. The data for Taurus was taken from Spezzano et al. (2013); Chantzios et al. (2018) and Giers et al. (2022). As the prestellar core L1544 appears in the three papers, we use the c-C₃H₂ D/H and D₂/D ratios derived from the latest work (Giers et al. 2022). The ra-

tios in these papers are not statistically corrected. Thus, for comparison purposes, we applied the same statistical factors used in this study (see Section 4.4).

All the ratios are plotted in statistically corrected percentages (Figure 13). For each singly- and doubly-deuterated ratio and molecular cloud a median value with uncertainties is computed. The uncertainties are computed with the same method used to calculate the otp ratio median uncertainty, and are plotted with horizontal dashed lines and bands. The Perseus median D/H value is $1.5 \pm 0.2 \%$, and the D₂/D median value is $25.9 \pm 4.3 \%$. The Taurus median D/H value is $4.8 \pm 0.5 \%$, and the D₂/D median value is $19.6 \pm 3.4 \%$. As for Chamaeleon there is just one measurement instead of the median, the corrected D/H value (12%) is given. The cores in Taurus have a larger c-C₃H₂ D/H ratio compared to the Perseus ones. The Cha-C2 prestellar core has a D/H value higher (12%) than the sources both in Perseus and Taurus. If the correlation between D/H and n_{H_2} is also present in the Taurus and Chamaeleon Molecular Clouds, the higher D/H ratio of Taurus and Chamaeleon (Cha-C2) compared to the one in Perseus would make sense as the cores in Taurus and in Chamaeleon have a higher median n_{H_2} (1.4×10^5 ³ and $5.5 \times 10^5 \text{ cm}^{-3}$, Chantzos et al. (2018); Belloche et al. (2011)) compared to the cores in Perseus. The D₂/D ratios are equivalent between the Perseus and Taurus Molecular Clouds. These results show there is greater variation of D/H and D₂/D ratios among cores within the same molecular cloud, than among the medians of different molecular clouds. Which suggests the local environment of the cores has a greater effect on the deuteration of c-C₃H₂ than the parent molecular cloud they are located in.

5.2.2. Comparison with Protostars

Besides studying the c-C₃H₂ deuteration towards starless and pre-stellar cores towards the Taurus Molecular Cloud in Chantzos et al. (2018), they also studied c-C₃HD and c-C₃D₂ towards some protostellar sources in the Taurus (L1521F) and Perseus (Per5, IRAS03282, HH211 and L1448-IRS2) Molecular Clouds. The mean derived D/H ratio towards the protostellar sources in the Perseus Molecular Cloud is $7 \pm 1 \%$, derived taking into account all Perseus sources mentioned above, and the D₂/D ratio is $34 \pm 6 \%$, derived from Per5 and HH211. These ratios take into account statistical corrections. The protostellar D/H median is higher than the starless and prestellar one derived in this study. This is likely due to the prestellar core that evolved into the observed protostars being longer lived than the starless and prestellar cores studied in this study. The protostellar D₂/D median is also higher than the one for starless and prestellar cores, but they agree within errors. They derived D/H and D₂/D ratios towards the L1521F protostellar core (Very Low Luminosity Object, or VeLLO) in the Taurus Molecular Cloud of $4 \pm 2 \%$ and $16 \pm 4 \%$. These ratios agree within errors with the mean values derived for starless and prestellar cores in Taurus. The protostellar D/H and D₂/D ratios generally agree

or are higher than the observed starless and prestellar ratios, suggesting at least a partial inheritance of the c-C₃H₂ budget, and supporting the idea that the deuterium fractionation increases throughout the prestellar core phase.

6. Conclusions

This work has presented new c-C₃H₂, c-C₃HD and c-C₃D₂ observations towards starless and prestellar cores towards the Perseus Molecular Cloud taken with the Yebes 40m, the ARO 12m and the IRAM 30m telescopes. c-C₃H₂ and c-C₃HD are detected towards all targeted cores except for Per752. c-C₃D₂ is detected towards 56% (9/16) of the targeted cores.

The ortho-to-para ratio of c-C₃H₂ has been studied leading to a median value of 3.5 ± 0.4 for all targeted cores. All targeted cores but Per799 (with a value of 4.7 ± 1.6) have a statistical otp ratio within uncertainties. No correlation has been found between c-C₃H₂ otp ratios and the evolutionary stage of the core, traced by n_{H_2} .

The median statistically corrected c-C₃H₂ D/H and D₂/D ratios derived from the observations are $1.5 \pm 0.2 \%$ and $25.9 \pm 4.3 \%$. No correlation has been found between D/H and D₂/D ratios. On the other hand, D/H ratios positively correlate with the core's volume density. This supports the idea that more evolved, and therefore, more dense cores, present higher levels of deuteration. The D₂/D ratios positively correlate with T_{kin} , suggesting that, while the first deuteration is dependent on volume density, the second deuteration is dependent on T_{kin} and may happen through slightly endothermic reactions. The median D/H ratio in Perseus is lower than the observed in cores towards the Taurus Molecular Cloud and the core observed towards the Chamaeleon Molecular Cloud. This could be attributed to the cores in the latter Molecular Clouds having higher n_{H_2} than the ones in Perseus. When it comes to D₂/D, even if the median found in Perseus is larger than in Taurus, they are equivalent taking uncertainties into account.

The variation of D/H and D₂/D ratios among cores is larger than the variation of their medians among molecular clouds, suggesting that the local environment of the cores have a higher impact on the deuteration of c-C₃H₂ than the parent cloud itself.

Acknowledgements. J. Ferrer Asensio thanks RIKEN Special Postdoctoral Researcher Program (Fellowships) for financial support. S. Scibelli acknowledges the National Radio Astronomy Observatory which is a facility of the National Science Foundation operated under cooperative agreement by Associated Universities, Inc. L. Steffes is supported by a National Science Foundation Graduate Research Fellowship Program under Grant N°[DGE-2137419]. Any opinions, findings, and conclusions or recommendations expressed in this material are those of the authors and do not necessarily reflect the views of the National Science Foundation. L. Steffes and Y. Shirley are also supported by the National Science Foundation Astronomy and Astrophysics Grant (AAG) AST-2205474. We are thankful to have the opportunity to conduct astronomical research on Iolkam Du'ag (Kitt Peak) in Arizona and we recognize and acknowledge the significant cultural role and reverence that these sites have to the Tohono O'odham Nation.

³ The Taurus starless and prestellar core volume densities are calculated in the same way as for the Perseus sources.

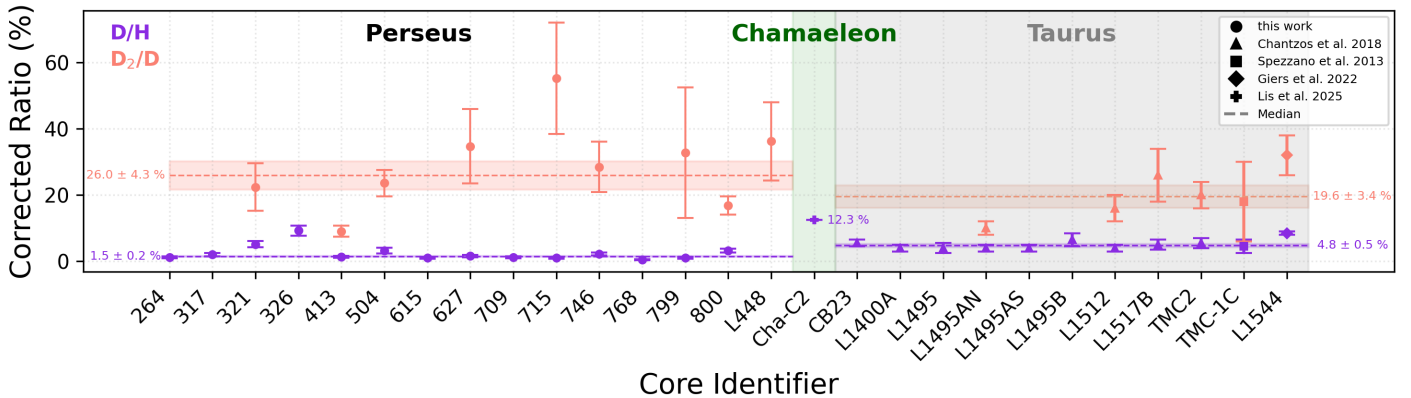


Fig. 13. Statistically corrected D/H and D₂/D ratios percentages for c-C₃H₂, in purple and orange, respectively, for the sources in the Perseus Molecular Cloud (this study, circles); and additional sources in the Chamaeleon Molecular Cloud: Cha-C2 (Lis et al. (2025), cross); Taurus Molecular Cloud, shaded in gray: CB23, L1400A, L1495, L1495AN, L1495AS, L1495B, L1512, L1517B and TMC2 (Chantzos et al. (2018), triangles); TMC-1C (Spezzano et al. (2013), square) and L1544 (Giers et al. (2022), diamond). The horizontal purple and orange dashed lines and bands, indicate the median with standard deviation for the D/H and D₂/D for the Perseus and the Taurus cores separately. For the Chamaeleon Molecular Cloud just one source, Cha-C2, is reported, so no median is given. Instead the value of the corrected D/H ratio is plotted.

We sincerely thank the operators of the Arizona Radio Observatory (Kevin Bays, Patrick Fimbrés, Blythe Guvenen, and Ryan Buchta) for their assistance with observations. The 12m Telescope is operated by the Arizona Radio Observatory (ARO), Steward Observatory, and the University of Arizona, with funding from the State of Arizona, NSF MRI Grant AST-1531366 (PI: Zuirys), NSF MSIP Grant SVS-85009 / AST-1653228 (PI: Marrone), NSF CAREER Grant AST-1653228 (PI: Marrone), and a PIRE Grant DISE-1743747 (PI: Psaltis). I. Jiménez-Serra and A. Megías acknowledge funding from the ERC grant OPENS (project number 101125858) funded by the European Union, and from the grant PID2022-136814NB-I00 funded by the Spanish Ministry of Science, Innovation and Universities / State Agency of Research, MCIU/AEI/10.13039/501100011033 and by "ERDF/EU". A. Taillard acknowledge funding from the European Research Council under the European Union's Horizon 2022 research and innovation program (grant agreement No. 101096293 SUL4LIFE).

References

Arce, H. G., Borkin, M. A., Goodman, A. A., Pineda, J. E., & Halle, M. W. 2010, ApJ, 715, 1170

Aspin, C., Sandell, G., & Russell, A. P. G. 1994, A&AS, 106, 165

Bell, M. B., Feldman, P. A., Matthews, H. E., & Avery, L. W. 1986, ApJ, 311, L89

Belloche, A., Parise, B., Schuller, F., et al. 2011, A&A, 535, A2

Ben Khalifa, M., Sahnoun, E., Wiesenfeld, L., et al. 2019, Physical Chemistry Chemical Physics (Incorporating Faraday Transactions), 21, 1443

Bergin, E. A. & Tafalla, M. 2007, ARA&A, 45, 339

Bogey, M., Demuynck, C., & Destombes, J. L. 1986, Chemical Physics Letters, 125, 383

Caselli, P., Keto, E., Bergin, E., et al. 2012, ApJ, 759, L37

Ceccarelli, C., Caselli, P., Bockelée-Morvan, D., et al. 2014, in Protostars and Planets VI, ed. H. Beuther, R. S. Klessen, C. P. Dullemond, & T. Henning, 859–882

Chantzos, J., Spezzano, S., Caselli, P., et al. 2018, ApJ, 863, 126

Cox, P., Guesten, R., & Henkel, C. 1988, A&A, 206, 108

Dislaire, V., Hily-Blant, P., Faure, A., et al. 2012, A&A, 537, A20

Drozdovskaya, M. N., Coudert, L. H., Margulès, L., et al. 2022, A&A, 659, A69

Enoch, M. L., Young, K. E., Glenn, J., et al. 2006, ApJ, 638, 293

Evans, II, N. J., Dunham, M. M., Jørgensen, J. K., et al. 2009, ApJS, 181, 321

Ferrer Asensio, J., Spezzano, S., Caselli, P., et al. 2022, A&A, 667, A119

Fuchs, G. W., Cuppen, H. M., Ioppolo, S., et al. 2009, A&A, 505, 629

Furuya, K., Aikawa, Y., Hincelin, U., et al. 2015, A&A, 584, A124

Gerin, M., Wootten, H. A., Combes, F., et al. 1987, A&A, 173, L1

Giers, K., Spezzano, S., Alves, F., et al. 2022, A&A, 664, A119

Ginsburg, A. & Mirocha, J. 2011, PySpecKit: Python Spectroscopic Toolkit, Astrophysics Source Code Library, record ascl:1109.001

Ginsburg, A., Sokolov, V., de Val-Borro, M., et al. 2022, AJ, 163, 291

Gratier, P., Majumdar, L., Ohishi, M., et al. 2016, ApJS, 225, 25

Gutermuth, R. A., Myers, P. C., Megeath, S. T., et al. 2008, ApJ, 674, 336

Hatchell, J., Richer, J. S., Fuller, G. A., et al. 2005, A&A, 440, 151

Hidaka, H., Watanabe, M., Kouchi, A., & Watanabe, N. 2009, ApJ, 702, 291

Higuchi, A. E., Sakai, N., Watanabe, Y., et al. 2018, ApJS, 236, 52

Jørgensen, J. K., Müller, H. S. P., Calcutt, H., et al. 2018, A&A, 620, A170

Keto, E. & Caselli, P. 2008, ApJ, 683, 238

Kirk, H., Johnstone, D., & Di Francesco, J. 2006, ApJ, 646, 1009

Kulterer, B. M., Fuente, A., Drozdovskaya, M. N., et al. 2025, arXiv e-prints, arXiv:2511.03581

Lada, E. A. & Lada, C. J. 1995, AJ, 109, 1682

Ladd, E. F., Lada, E. A., & Myers, P. C. 1993, ApJ, 410, 168

Lin, Y., Spezzano, S., & Caselli, P. 2023, A&A, 669, L6

Linsky, J. L. 2003, Space Sci. Rev., 106, 49

Lis, D. C., Langer, W. D., Pineda, J. L., et al. 2025, A&A, 696, A61

Loison, J.-C., Agúndez, M., Wakelam, V., et al. 2017, MNRAS, 470, 4075

Lovas, F. J., Suenram, R. D., Ogata, T., & Yamamoto, S. 1992, ApJ, 399, 325

Lucas, R. & Liszt, H. S. 2000, A&A, 358, 1069

Lupi, A., Bovino, S., & Grassi, T. 2021, A&A, 654, L6

Madden, S. C., Irvine, W. M., Matthews, H. E., Friberg, P., & Swade, D. A. 1989, AJ, 97, 1403

Majumdar, L., Gratier, P., Andron, I., Wakelam, V., & Caux, E. 2017, MNRAS, 467, 3525

Manigand, S., Jørgensen, J. K., Calcutt, H., et al. 2020, A&A, 635, A48

Martínez-Henares, A., Jiménez-Serra, I., Vastel, C., et al. 2025, A&A, 699, A382

Megías, A., Jiménez-Serra, I., Martín-Pintado, J., et al. 2023, MNRAS, 519, 1601

Melosso, M., Bizzocchi, L., Sipilä, O., et al. 2020, A&A, 641, A153

Morisawa, Y., Fushitani, M., Kato, Y., et al. 2006, ApJ, 642, 954

Muench, A. A., Lada, C. J., Luhman, K. L., Muzerolle, J., & Young, E. 2007, AJ, 134, 411

Osamura, Y., Roberts, H., & Herbst, E. 2004, A&A, 421, 1101

Pagani, L., Salez, M., & Wannier, P. G. 1992, A&A, 258, 479

Pagani, L., Vastel, C., Hugo, E., et al. 2009, A&A, 494, 623

Park, I. H., Herbst, E., Morisawa, Y., & Momose, T. 2005, in IAU Symposium, Vol. 231, Astrochemistry: Recent Successes and Current Challenges, ed. D. C. Lis, G. A. Blake, & E. Herbst, 32

Pety, J. 2005, in SF2A-2005: Semaine de l’Astrophysique Française, ed. F. Casoli, T. Contini, J. M. Hameury, & L. Pagani, 721

Pezzuto, S., Benedettini, M., Di Francesco, J., et al. 2021, A&A, 645, A55

Pezzuto, S., Elia, D., Schisano, E., et al. 2012, A&A, 547, A54

Prodanović, T., Steigman, G., & Fields, B. D. 2010, MNRAS, 406, 1108

Richard, C., Jørgensen, J. K., Margulès, L., et al. 2021, A&A, 651, A120

Rodríguez-Baras, M., Esplugues, G., Fuente, A., et al. 2023, A&A, 679, A120

Rodríguez-Baras, M., Fuente, A., Riviére-Marichalar, P., et al. 2021, A&A, 648, A120

Sadavoy, S. I., di Francesco, J., André, P., et al. 2012, A&A, 540, A10

Sadavoy, S. I., Di Francesco, J., André, P., et al. 2014, ApJ, 787, L18

Scibelli, S., Drozdovskaya, M. N., Caselli, P., et al. 2025, A&A, 702, A127

Scibelli, S., Shirley, Y., Megías, A., & Jiménez-Serra, I. 2024, MNRAS, 533, 4104

Spezzano, S., Brünken, S., Schilke, P., et al. 2013, ApJ, 769, L19

Spezzano, S., Sipilä, O., Caselli, P., et al. 2022, A&A, 661, A111

Spezzano, S., Tamassia, F., Thorwirth, S., et al. 2012, ApJS, 200, 1

Takakuwa, S., Kawaguchi, K., Mikami, H., & Saito, M. 2001, PASJ, 53, 251

Tercero, F., López-Pérez, J. A., Gallego, J. D., et al. 2021, A&A, 645, A37

Thaddeus, P., Vrtilek, J. M., & Gottlieb, C. A. 1985, ApJ, 299, L63

van der Tak, F. F. S., Black, J. H., Schöier, F. L., Jansen, D. J., & van Dishoeck, E. F. 2007, A&A, 468, 627

van Gelder, M. L., Jaspers, J., Nazari, P., et al. 2022, A&A, 667, A136

Vrtilek, J. M., Gottlieb, C. A., & Thaddeus, P. 1987, ApJ, 314, 716

Watanabe, N., Hidaka, H., Nagaoka, A., & Kouchi, A. 2005, in IAU Symposium, Vol. 231, Astrochemistry: Recent Successes and Current Challenges, ed. D. C. Lis, G. A. Blake, & E. Herbst, 182

Watanabe, N. & Kouchi, A. 2002, ApJ, 571, L173

Yang, Y.-L., Sakai, N., Zhang, Y., et al. 2021, ApJ, 910, 20

Zari, E., Lombardi, M., Alves, J., Lada, C. J., & Bouy, H. 2016, A&A, 587, A106

Zucker, C., Schlafly, E. F., Speagle, J. S., et al. 2018, ApJ, 869, 83

Appendix A: Observed Transitions

The observed c-C₃H₂, c-C₃HD and c-C₃D₂ transitions are presented in Tables A.1, A.2 and A.3, respectively. The peak temperature (T_{MB}), position (V_{LSR}), width (FWHM), rms and signal-to-noise ratio (SNR), calculated with the peak intensity, of the lines are given. The transitions that could not be fitted with pyspeckit are marked with an asterisk (*). For these transitions we provide the peak temperature, derived from the integrated area and an assumed FWHM value which is also indicated.

Table A.1. Observed c-C₃H₂ transitions.

Core	Transition	T_{MB} (mK)	V_{LSR} (km s ⁻¹)	FWHM (km s ⁻¹)	rms (mK)	SNR
264	3 ₂₁ - 3 ₁₂	45	7.996 (0.006)	0.622 (0.015)	6	7
	2 ₁₁ - 2 ₀₂	196	7.915 (0.001)	0.508 (0.003)	6	34
	2 ₂₀ - 1 ₁₁	152	7.916 (0.001)	0.481 (0.003)	19	8
	4 ₀₄ - 3 ₁₃	131	7.928 (0.001)	0.460 (0.003)	18	7
	3 ₁₂ - 2 ₂₁	338	7.937 (0.000)	0.502 (0.001)	39	9
	4 ₁₄ - 3 ₀₃	381	8.028 (0.000)	0.488 (0.001)	20	19
317	3 ₂₁ - 3 ₁₂	23	8.036 (0.012)	0.824 (0.029)	5	4
	2 ₁₁ - 2 ₀₂	64	8.253 (0.004)	0.619 (0.010)	7	9
	2 ₂₀ - 1 ₁₁	59	8.226 (0.004)	0.766 (0.009)	12	5
	4 ₀₄ - 3 ₁₃	60	8.319 (0.003)	0.671 (0.008)	11	5
	3 ₁₂ - 2 ₂₁	150	8.262 (0.001)	0.510 (0.003)	23	7
	4 ₁₄ - 3 ₀₃	168	8.397 (0.001)	0.637 (0.003)	18	9
321	3 ₂₁ - 3 ₁₂	38	8.430 (0.007)	0.572 (0.016)	4	9
	2 ₁₁ - 2 ₀₂	65	8.371 (0.005)	0.781 (0.012)	6	10
	2 ₂₀ - 1 ₁₁	71	8.542 (0.003)	0.659 (0.006)	15	5
	4 ₀₄ - 3 ₁₃	121	8.629 (0.002)	0.664 (0.004)	21	6
	3 ₁₂ - 2 ₂₁	260	8.560 (0.001)	0.437 (0.001)	33	8
	4 ₁₄ - 3 ₀₃	325	8.576 (0.001)	0.591 (0.001)	21	15
326	3 ₂₁ - 3 ₁₂	64	7.958 (0.005)	0.801 (0.011)	3	20
	2 ₁₁ - 2 ₀₂	120	7.962 (0.003)	0.935 (0.007)	6	21
	2 ₂₀ - 1 ₁₁	160	8.188 (0.001)	0.604 (0.003)	18	9
	4 ₀₄ - 3 ₁₃	170	8.134 (0.001)	0.854 (0.003)	27	6
	3 ₁₂ - 2 ₂₁	364	8.151 (0.001)	0.651 (0.001)	37	10
	4 ₁₄ - 3 ₀₃	502	8.149 (0.000)	0.846 (0.001)	22	23
413	3 ₂₁ - 3 ₁₂	94	7.773 (0.003)	0.620 (0.007)	7	14
	2 ₁₁ - 2 ₀₂	508	7.785 (0.000)	0.534 (0.001)	7	76
	2 ₂₀ - 1 ₁₁	353	7.786 (0.000)	0.396 (0.001)	27	13
	4 ₀₄ - 3 ₁₃	432	7.840 (0.000)	0.346 (0.001)	27	16
	3 ₁₂ - 2 ₂₁	806	7.797 (0.000)	0.414 (0.000)	49	17
	4 ₁₄ - 3 ₀₃	717	7.845 (0.000)	0.437 (0.000)	32	22
504	3 ₂₁ - 3 ₁₂	42	6.775 (0.005)	0.454 (0.013)	2	18
	2 ₁₁ - 2 ₀₂	220	6.742 (0.001)	0.476 (0.002)	4	49
	2 ₂₀ - 1 ₁₁	154	6.749 (0.001)	0.257 (0.001)	34	5
	4 ₀₄ - 3 ₁₃	180	6.793 (0.001)	0.242 (0.001)	22	8
	3 ₁₂ - 2 ₂₁	398	6.791 (0.000)	0.307 (0.001)	41	10
	4 ₁₄ - 3 ₀₃	355	6.816 (0.000)	0.279 (0.001)	32	11
615	3 ₂₁ - 3 ₁₂	20	7.956 (0.011)	0.449 (0.025)	6	3
	2 ₁₁ - 2 ₀₂	178	8.106 (0.001)	0.503 (0.003)	5	33
	2 ₂₀ - 1 ₁₁	87	8.062 (0.002)	0.474 (0.004)	13	7
	4 ₀₄ - 3 ₁₃	82	8.084 (0.002)	0.436 (0.004)	11	7
	3 ₁₂ - 2 ₂₁	249	8.063 (0.001)	0.402 (0.001)	39	6
	4 ₁₄ - 3 ₀₃	199	8.172 (0.001)	0.383 (0.001)	13	15
627	3 ₂₁ - 3 ₁₂	48	8.380 (0.006)	0.338 (0.009)	6	8
	2 ₁₁ - 2 ₀₂	178	8.460 (0.001)	0.375 (0.003)	8	21
	2 ₂₀ - 1 ₁₁	139	8.394 (0.001)	0.321 (0.002)	21	7
	4 ₀₄ - 3 ₁₃	155	8.388 (0.001)	0.332 (0.002)	30	5
	3 ₁₂ - 2 ₂₁	285	8.411 (0.000)	0.290 (0.001)	48	6
	4 ₁₄ - 3 ₀₃	247	8.471 (0.000)	0.365 (0.001)	23	11

Table A.1. Observed c-C₃H₂ transitions (continued).

Core	Transition	T_{MB} (mK)	V_{LSR} (km s ⁻¹)	FWHM (km s ⁻¹)	rms (mK)	SNR
709	3 ₂₁ - 3 ₁₂	30	8.519 (0.010)	0.797 (0.024)	6	5
	2 ₁₁ - 2 ₀₂	81	8.589 (0.004)	0.981 (0.009)	6	13
	2 ₂₀ - 1 ₁₁	78	8.487 (0.003)	0.760 (0.006)	24	3
	4 ₀₄ - 3 ₁₃	85	8.547 (0.002)	0.860 (0.006)	16	5
	3 ₁₂ - 2 ₂₁	199	8.513 (0.001)	0.842 (0.003)	31	6
	4 ₁₄ - 3 ₀₃	244	8.538 (0.001)	0.915 (0.003)	14	18
715	3 ₂₁ - 3 ₁₂	30	8.826 (0.011)	0.782 (0.026)	4	8
	2 ₁₁ - 2 ₀₂	119	8.923 (0.002)	0.624 (0.006)	5	22
	2 ₂₀ - 1 ₁₁	82	8.913 (0.003)	0.632 (0.006)	14	6
	4 ₀₄ - 3 ₁₃	83	9.039 (0.001)	0.239 (0.003)	13	6
	3 ₁₂ - 2 ₂₁	201	8.917 (0.001)	0.621 (0.002)	55	4
	4 ₁₄ - 3 ₀₃	262	9.085 (0.000)	0.230 (0.001)	12	21
746	3 ₂₁ - 3 ₁₂	48	8.923 (0.006)	0.362 (0.008)	7	7
	2 ₁₁ - 2 ₀₂	190	8.892 (0.001)	0.484 (0.003)	8	24
	2 ₂₀ - 1 ₁₁	95	8.927 (0.001)	0.389 (0.003)	18	5
	4 ₀₄ - 3 ₁₃	111	9.028 (0.001)	0.252 (0.002)	18	6
	3 ₁₂ - 2 ₂₁	289	8.992 (0.000)	0.370 (0.001)	33	9
	4 ₁₄ - 3 ₀₃	260	9.039 (0.000)	0.321 (0.001)	28	9
768	3 ₂₁ - 3 ₁₂	76	8.906 (0.003)	0.557 (0.008)	4	21
	2 ₁₁ - 2 ₀₂	265	8.931 (0.001)	0.615 (0.002)	3	86
	2 ₂₀ - 1 ₁₁	267	9.004 (0.000)	0.344 (0.001)	47	6
	4 ₀₄ - 3 ₁₃	321	9.138 (0.000)	0.379 (0.001)	44	7
	3 ₁₂ - 2 ₂₁	523	9.049 (0.000)	0.420 (0.001)	60	9
	4 ₁₄ - 3 ₀₃	610	9.105 (0.000)	0.461 (0.001)	47	13
799	*3 ₂₁ - 3 ₁₂	41		0.025	5	8
	2 ₁₁ - 2 ₀₂	259	10.146 (0.001)	0.386 (0.002)	7	39
	2 ₂₀ - 1 ₁₁	170	10.213 (0.001)	0.250 (0.001)	16	10
	4 ₀₄ - 3 ₁₃	74	10.240 (0.001)	0.246 (0.003)	17	4
	3 ₁₂ - 2 ₂₁	367	10.219 (0.000)	0.339 (0.001)	54	7
	4 ₁₄ - 3 ₀₃	363	10.277 (0.000)	0.247 (0.001)	26	14
800	3 ₂₁ - 3 ₁₂	89	10.310 (0.003)	0.564 (0.007)	6	16
	2 ₁₁ - 2 ₀₂	310	10.316 (0.001)	0.572 (0.002)	5	60
	2 ₂₀ - 1 ₁₁	185	10.421 (0.001)	0.735 (0.002)	29	6
	4 ₀₄ - 3 ₁₃	234	10.528 (0.001)	0.470 (0.001)	28	8
	3 ₁₂ - 2 ₂₁	572	10.463 (0.000)	0.429 (0.001)	47	12
	4 ₁₄ - 3 ₀₃	503	10.516 (0.000)	0.494 (0.001)	32	16

Table A.2. Observed c-C₃HD transitions.

Core	Transition	T_{MB} (mK)	V_{LSR} (km s ⁻¹)	FWHM (km s ⁻¹)	rms (mK)	SNR
264	2 ₁₁ - 2 ₀₂	21	7.935 (0.013)	0.590 (0.030)	2	11
	1 ₁₁ - 0 ₀₀	44	8.011 (0.006)	0.677 (0.014)	12	4
	4 ₁₄ - 3 ₀₃	43	7.985 (0.004)	0.514 (0.009)	6	7
	2 ₂₀ - 1 ₁₁	34	8.035 (0.005)	0.511 (0.011)	6	6
317	2 ₁₁ - 2 ₀₂	14	8.280 (0.020)	0.605 (0.048)	3	5
	1 ₁₁ - 0 ₀₀	38	8.210 (0.006)	0.465 (0.013)	9	4
	4 ₁₄ - 3 ₀₃	33	8.315 (0.003)	0.273 (0.008)	9	4
	2 ₂₀ - 1 ₁₁	28	8.459 (0.005)	0.430 (0.012)	8	3
321	2 ₁₁ - 2 ₀₂	15	8.539 (0.019)	0.562 (0.043)	3	6
	1 ₁₁ - 0 ₀₀	23	8.366 (0.009)	0.540 (0.022)	7	4
	4 ₁₄ - 3 ₀₃	57	8.523 (0.003)	0.489 (0.007)	11	5
	2 ₂₀ - 1 ₁₁	162	8.508 (0.003)	0.439 (0.008)	11	15
326	2 ₁₁ - 2 ₀₂	24	7.998 (0.015)	0.979 (0.036)	2	12
	1 ₀₁ - 0 ₀₀	10	7.850 (0.030)	0.807 (0.071)	2	4
	1 ₁₁ - 0 ₀₀	74	8.061 (0.004)	0.652 (0.009)	6	12
	4 ₁₄ - 3 ₀₃	71	8.087 (0.003)	0.936 (0.007)	13	5
	2 ₂₀ - 1 ₁₁	173	8.157 (0.004)	0.969 (0.009)	13	13
413	2 ₁₁ - 2 ₀₂	77	7.816 (0.004)	0.635 (0.009)	4	22
	1 ₀₁ - 0 ₀₀	27	7.896 (0.013)	0.855 (0.030)	4	7
	1 ₁₁ - 0 ₀₀	240	7.874 (0.001)	0.627 (0.003)	8	31
	4 ₁₄ - 3 ₀₃	141	7.779 (0.001)	0.285 (0.002)	13	11
	2 ₂₀ - 1 ₁₁	146	7.823 (0.001)	0.342 (0.002)	12	13
504	2 ₁₁ - 2 ₀₂	46	6.783 (0.006)	0.629 (0.015)	2	19
	1 ₀₁ - 0 ₀₀	21	6.718 (0.013)	0.701 (0.032)	3	6
	1 ₁₁ - 0 ₀₀	150	6.788 (0.002)	0.573 (0.004)	8	20
	4 ₁₄ - 3 ₀₃	90	6.703 (0.001)	0.249 (0.002)	13	7
	2 ₂₀ - 1 ₁₁	91	6.755 (0.001)	0.319 (0.003)	11	9
615	2 ₁₁ - 2 ₀₂	23	8.080 (0.011)	0.584 (0.027)	2	12
	1 ₁₁ - 0 ₀₀	82	8.175 (0.003)	0.504 (0.006)	11	8
	4 ₁₄ - 3 ₀₃	17	8.051 (0.012)	0.559 (0.028)	6	3
	2 ₂₀ - 1 ₁₁	28	8.158 (0.004)	0.348 (0.010)	7	4
627	2 ₁₁ - 2 ₀₂	26	8.348 (0.011)	0.535 (0.023)	3	8
	1 ₁₁ - 0 ₀₀	118	8.507 (0.002)	0.525 (0.005)	10	12
	4 ₁₄ - 3 ₀₃	39	8.331 (0.003)	0.259 (0.006)	6	7
	2 ₂₀ - 1 ₁₁	55	8.400 (0.002)	0.308 (0.005)	6	9
709	2 ₁₁ - 2 ₀₂	18	8.521 (0.017)	0.747 (0.040)	3	5
	1 ₁₁ - 0 ₀₀	46	8.390 (0.006)	0.680 (0.014)	8	6
	4 ₁₄ - 3 ₀₃	26	8.445 (0.007)	0.631 (0.016)	5	6
	2 ₂₀ - 1 ₁₁	25	8.441 (0.008)	0.670 (0.018)	5	5
715	2 ₁₁ - 2 ₀₂	15	8.774 (0.026)	0.826 (0.060)	2	7
	1 ₁₁ - 0 ₀₀	38	8.951 (0.008)	0.698 (0.018)	10	4
	4 ₁₄ - 3 ₀₃	24	9.008 (0.004)	0.212 (0.009)	4	5
	2 ₂₀ - 1 ₁₁	27	9.055 (0.004)	0.263 (0.010)	5	5
746	2 ₁₁ - 2 ₀₂	34	8.952 (0.008)	0.514 (0.018)	3	12
	1 ₁₁ - 0 ₀₀	122	8.966 (0.002)	0.520 (0.005)	8	15
	4 ₁₄ - 3 ₀₃	43	9.028 (0.006)	0.748 (0.014)	7	6
	2 ₂₀ - 1 ₁₁	35	8.995 (0.004)	0.407 (0.010)	8	4
768	2 ₁₁ - 2 ₀₂	19	8.914 (0.014)	0.495 (0.028)	2	9
	1 ₁₁ - 0 ₀₀	62	8.978 (0.004)	0.561 (0.009)	4	14
	4 ₁₄ - 3 ₀₃	37	9.047 (0.003)	0.336 (0.007)	7	6
	2 ₂₀ - 1 ₁₁	45	9.108 (0.003)	0.426 (0.007)	5	8

Table A.2. Observed c-C₃HD transitions (continued).

Core	Transition	T_{MB} (mK)	V_{LSR} (km s ⁻¹)	FWHM (km s ⁻¹)	rms (mK)	SNR
799	2 ₁₁ - 2 ₀₂	39	10.135 (0.008)	0.385 (0.019)	3	12
	1 ₁₁ - 0 ₀₀	138	10.192 (0.002)	0.511 (0.004)	12	11
	4 ₁₄ - 3 ₀₃	46	10.195 (0.002)	0.217 (0.005)	5	8
	2 ₂₀ - 1 ₁₁	58	10.274 (0.002)	0.263 (0.004)	4	15
800	2 ₁₁ - 2 ₀₂	68	10.336 (0.005)	0.716 (0.011)	3	22
	1 ₀₁ - 0 ₀₀	27	10.322 (0.012)	0.821 (0.028)	4	6
	1 ₁₁ - 0 ₀₀	233	10.382 (0.001)	0.633 (0.003)	10	24
	4 ₁₄ - 3 ₀₃	93	10.418 (0.001)	0.491 (0.003)	9	10
	2 ₂₀ - 1 ₁₁	106	10.476 (0.001)	0.522 (0.004)	11	10
L1448	3 ₀₃ - 2 ₀₂	33	4.676 (0.005)	0.353 (0.011)	4	8

Table A.3. Observed c-C₃D₂ transitions.

Core	Transition	T_{MB} (mK)	V_{LSR} (km s ⁻¹)	FWHM (km s ⁻¹)	rms (mK)	SNR
321	1 ₁₁ - 0 ₀₀	13	8.537 (0.019)	0.586 (0.045)	4	3
413	1 ₁₁ - 0 ₀₀	23	7.904 (0.009)	0.504 (0.024)	4	6
504	2 ₁₁ - 2 ₀₂	7	6.690 (0.051)	0.836 (0.119)	2	4
	1 ₁₁ - 0 ₀₀	34	6.867 (0.007)	0.548 (0.018)	4	9
627	* 1 ₁₁ - 0 ₀₀	35		0.25	5	7
715	1 ₁₁ - 0 ₀₀	13	9.082 (0.020)	0.552 (0.046)	4	4
746	1 ₁₁ - 0 ₀₀	26	8.939 (0.008)	0.475 (0.022)	6	4
799	* 1 ₁₁ - 0 ₀₀	29		0.25	5	6
800	2 ₁₁ - 2 ₀₂	9	10.325 (0.035)	0.876 (0.084)	2	4
	1 ₁₁ - 0 ₀₀	42	10 (0.005)	0.479 (0.013)	6	7
L1448	3 ₀₃ - 2 ₁₂	29	4.965 (0.005)	0.300 (0.011)	4	7

Appendix B: Column Density calculation

With the aim of testing the viability of using fixed values for n_{H_2} and T_{kin} to compute the column density of c-C₃H₂ and its isotopologues with RADEX, we computed the column density for two transitions for a grid of n_{H_2} and T_{kin} values. An example core was selected, Per317, and the column density for the ortho-c-C₃H₂ 3_{2,1} - 3_{1,2} and para-c-C₃H₂ 2_{1,1} - 2_{0,2} transitions were calculated for a n_{H_2} range of 0.25 - 1.75 $\times 10^5$ cm⁻³ and for a T_{kin} range of 10 - 21 K (Figures B.1 and B.2, respectively). The obtained column density values within the 10% observational uncertainty of the constrained n_{H_2} and T_{kin} values taken from Scibelli et al. (2024), varies by less than a factor of 2. Thus, the approach of fixing the n_{H_2} and T_{kin} values while taking into account a 10% observational uncertainty, is a reasonable assumption to derive the column densities of c-C₃H₂ and its isotopologues.

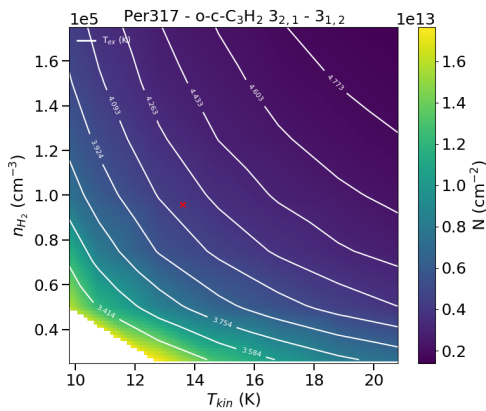


Fig. B.1. Column density of the ortho-c-C₃H₂ 3_{2,1} - 3_{1,2} transition of Per317 plotted with a colour gradient for a range of n_{H_2} and T_{kin} . The contour white lines indicate the excitation temperature of the transition, T_{ex} , and the red cross marks the n_{H_2} and T_{kin} values derived in Pezzuto et al. (2021).

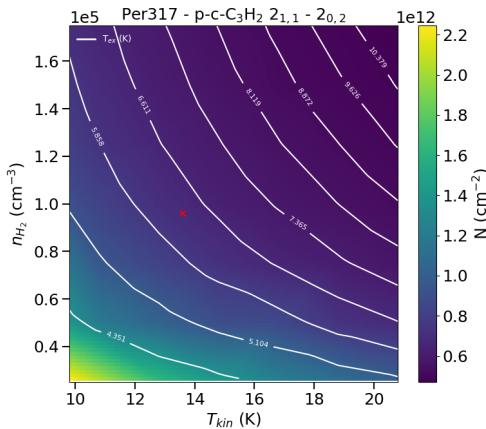


Fig. B.2. Column density of the para-c-C₃H₂ 2_{1,1} - 2_{0,2} transition of Per317 plotted with a colour gradient for a range of n_{H_2} and T_{kin} . The contour white lines indicate the excitation temperature of the transition, T_{ex} , and the red cross marks the n_{H_2} and T_{kin} values derived in Pezzuto et al. (2021).

B.1. Output n_{H_2} and T_{kin}

We report the constrained n_{H_2} and T_{kin} by RADEX for each of the molecules: orhto-c-C₃H₂, para-c-C₃H₂, c-C₃HD and ortho-c-C₃D₂ (Tables B.1, B.2, B.3 and B.4, respectively). As seen above, the column density does not change significantly within the 10% error assumed for n_{H_2} and T_{kin} . That is why the standard deviation of the volume density and kinetic temperature range within this 10% uncertainty, and thus why the values are not tightly constrained.

Table B.1. Constrained n_{H_2} and T_{kin} from the RADEX fitting of ortho-c-C₃H₂.

Core	n_{H_2} (cm ⁻³)	T_{kin} (K)
264	$7.5 \pm 0.7 \times 10^4$	11 ± 1
317	$9.4 \pm 0.9 \times 10^4$	14 ± 1
321	$1.3 \pm 0.1 \times 10^5$	12 ± 1
326	$2.9 \pm 0.3 \times 10^5$	12 ± 1
413	$4.2 \pm 0.4 \times 10^4$	11 ± 1
504	$6.5 \pm 0.7 \times 10^4$	10 ± 1
615	$3.5 \pm 0.3 \times 10^4$	10 ± 1
627	$3.2 \pm 0.3 \times 10^4$	12 ± 1
709	$5.1 \pm 0.5 \times 10^4$	14 ± 1
715	$4.9 \pm 0.5 \times 10^4$	15 ± 2
746	$4.9 \pm 0.5 \times 10^4$	11 ± 1
768	$4.9 \pm 0.5 \times 10^4$	11 ± 1
799	$3.3 \pm 0.3 \times 10^4$	10 ± 1
800	$6.4 \pm 0.7 \times 10^4$	12 ± 1

Table B.2. Constrained n_{H_2} and T_{kin} from the RADEX fitting of para-c-C₃H₂.

Core	n_{H_2} (cm ⁻³)	T_{kin} (K)
264	$7.5 \pm 0.7 \times 10^4$	11 ± 1
317	$9.7 \pm 0.9 \times 10^4$	13 ± 1
321	$1.3 \pm 0.1 \times 10^5$	13 ± 1
326	$2.6 \pm 0.2 \times 10^5$	12 ± 1
413	$4.2 \pm 0.4 \times 10^4$	10 ± 1
504	$6.5 \pm 0.6 \times 10^4$	10 ± 1
615	$3.4 \pm 0.3 \times 10^4$	10 ± 1
627	$3.2 \pm 0.3 \times 10^4$	12 ± 1
709	$5.1 \pm 0.6 \times 10^4$	13 ± 1
715	$4.9 \pm 0.5 \times 10^4$	15 ± 1
746	$4.9 \pm 0.5 \times 10^4$	11 ± 1
768	$4.9 \pm 0.5 \times 10^4$	11 ± 1
799	$3.3 \pm 0.3 \times 10^4$	10 ± 1
800	$6.4 \pm 0.6 \times 10^4$	11 ± 1

Table B.3. Constrained n_{H_2} and T_{kin} from the RADEX fitting of c-C₃HD.

Core	n_{H_2} (cm ⁻³)	T_{kin} (K)
264	$7.5 \pm 0.8 \times 10^4$	11 ± 1
317	$9.6 \pm 1.0 \times 10^4$	14 ± 1
321	$1.3 \pm 0.1 \times 10^5$	13 ± 1
326	$2.8 \pm 0.3 \times 10^5$	12 ± 1
413	$4.2 \pm 0.4 \times 10^4$	10 ± 1
504	$6.5 \pm 0.7 \times 10^4$	10 ± 1
615	$3.5 \pm 0.3 \times 10^4$	10 ± 1
627	$3.2 \pm 0.3 \times 10^4$	12 ± 1
709	$5.1 \pm 0.5 \times 10^4$	14 ± 1
715	$4.9 \pm 0.4 \times 10^4$	15 ± 1
746	$4.8 \pm 0.5 \times 10^4$	11 ± 1
768	$4.8 \pm 0.5 \times 10^4$	11 ± 1
799	$3.3 \pm 0.4 \times 10^4$	10 ± 1
800	$6.3 \pm 0.6 \times 10^4$	12 ± 1
L448	$5.7 \pm 0.6 \times 10^4$	15 ± 1

Appendix C: Fractional Abundance

The fractional abundance of c-C₃H₂, c-C₃HD and c-C₃D₂ with respect to molecular hydrogen are plotted for the studied starless and prestellar cores in the Perseus Molecular Cloud (Figure C.1).

Table B.4. Constrained n_{H_2} and T_{kin} from the RADEX fitting of ortho-c-C₃D₂.

Core	n_{H_2} (cm ⁻³)	T_{kin} (K)
321	$(1.3 \pm 0.1) \times 10^5$	13 ± 1
413	$(4.2 \pm 0.4) \times 10^4$	11 ± 1
504	$(6.5 \pm 0.7) \times 10^4$	10 ± 1
627	$(3.2 \pm 0.3) \times 10^4$	12 ± 1
715	$(4.9 \pm 0.5) \times 10^4$	15 ± 2
746	$(4.9 \pm 0.5) \times 10^4$	11 ± 1
799	$(3.3 \pm 0.3) \times 10^4$	10 ± 1
800	$(6.4 \pm 0.7) \times 10^4$	12 ± 1

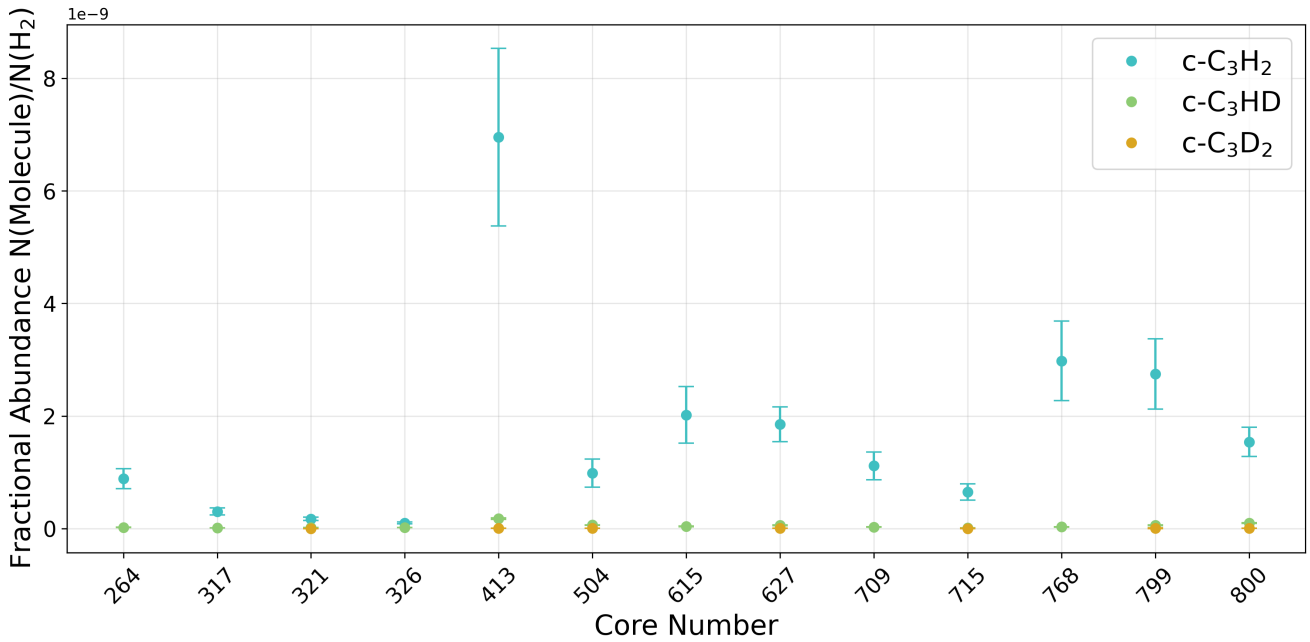


Fig. C.1. Abundance of c-C₃H₂, c-C₃HD and c-C₃D₂ with respect to molecular hydrogen in blue, green and orange, respectively.